

## Accepted Manuscript

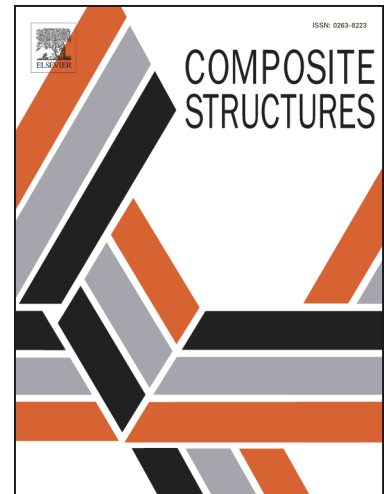
Vibration control and analysis of a rotating flexible FGM beam with a lumped mass in temperature field

Liang Li, Wei-Hsin Liao, Dingguo Zhang, Yang Zhang

PII: S0263-8223(18)31640-4  
DOI: <https://doi.org/10.1016/j.compstruct.2018.09.070>  
Reference: COST 10216

To appear in: *Composite Structures*

Received Date: 7 May 2018  
Revised Date: 20 August 2018  
Accepted Date: 19 September 2018



Please cite this article as: Li, L., Liao, W-H., Zhang, D., Zhang, Y., Vibration control and analysis of a rotating flexible FGM beam with a lumped mass in temperature field, *Composite Structures* (2018), doi: <https://doi.org/10.1016/j.compstruct.2018.09.070>

This is a PDF file of an unedited manuscript that has been accepted for publication. As a service to our customers we are providing this early version of the manuscript. The manuscript will undergo copyediting, typesetting, and review of the resulting proof before it is published in its final form. Please note that during the production process errors may be discovered which could affect the content, and all legal disclaimers that apply to the journal pertain.

# Vibration control and analysis of a rotating flexible FGM beam with a lumped mass in temperature field

Liang Li<sup>a,b</sup>, Wei-Hsin Liao<sup>a,\*</sup>, Dingguo Zhang<sup>b</sup>, Yang Zhang<sup>b</sup>

<sup>a</sup>Department of Mechanical and Automation Engineering, The Chinese University of Hong Kong, Hong Kong, China

<sup>b</sup>School of Science, Nanjing University of Science and Technology, Nanjing 210094, China

**Abstract:** Based on the high-order coupling (HOC) modelling theory, vibration control of a rotating rigid-flexible coupled smart composite structure in temperature field is investigated. A flexible beam made of functionally graded materials (FGM) with a lumped mass and two piezoelectric films perfectly bonded to it is attached to a horizontal rotating hub. By using the method of assumed modes to describe the deformations of the FGM beam and piezoelectric films, the rigid-flexible coupling dynamic equations of the system with the high order geometric nonlinear terms are derived via employing Lagrange's equations. A PD controller is used in the vibration control of the system. Simulation results indicate that the intense thermally induced vibrations of the FGM beam along the longitudinal and transverse direction are efficiently suppressed after the piezoelectric active control effect works. The HOC model is more accurate than the previous low order coupled (LOC) model when the temperature gradient increases. The influence of high-order nonlinearity in the present HOC model on the characteristics of dynamics and control of flexible structures should not be ignored. The effect of temperature variation on the free vibration characteristics of the rotating smart structure is gentle despite non-negligibility.

**Keywords:** functionally graded materials, rotating smart structures, temperature field, vibration control

## 1 Introduction

Functionally graded materials (FGMs) are one type of advanced composites which has remarkable properties and promising applications in the field of spacecraft, nuclear industries, and other engineering applications. The FGMs, formed by continuous graduation of two or more constituent phases over a specified volume, were mainly designed and developed to resist high temperature gradients.

Gupta and Talha [1] made a comprehensive literature review on structural characteristics of FGM structures under thermo-electro-mechanical loadings, and provided an overview of the future research directions in the design and analysis of FGMs. He et al. [2] introduced the finite element formulation based on thin plate theory to control the shape and vibration of FGM plate with integrated piezoelectric sensors and actuators under mechanical load. Liew et al. [3] investigated postbuckling and thermal postbuckling behavior of FGM plates with two opposite edges fixed and with surface-bonded piezoelectric actuators. Huang and Shen [4] studied the effects of temperature change, voltage and volume fraction distribution on the nonlinear vibration and dynamic response of FGM plate under thermo-electro loading. Shen [5] studied the nonlinear thermal bending response and postbuckling of FGMs plates with piezoelectric actuators under thermal and electrical loads. Fakhari et al. [6] studied nonlinear natural frequencies and dynamic responses of FGM plates with surface bonded piezoelectric layers based on HSDT. Jia et al. [7] made thermal-mechanical-electrical buckling analysis of micro-FGM beams by using the modified couple stress theory. Wang and Shen [8] studied the nonlinear vibration of functionally graded graphene reinforced composite (FG-GRC) face sheets in thermal environments.

Since researchers are mainly focused their study on transient analysis of FGM structures under thermo-electro-mechanical environments, there are limited contributions on dynamics analysis of FGM structures undergoing large overall rotating motion. Librescu et al. [9] studied the modeling and vibrations of FGM thin walled rotating beams. The thermal field considered in their study was assumed steady state. Fazelzadeh et al. [10] investigated the dynamic characteristics of a rotating thin-walled blade made of FGMs in high temperature, supersonic gas flow by using the differential quadrature method. Piovan and Sampaio [11] introduced a new finite element to study the dynamic behavior of rotating FGM beams. Zarrinzadeh et al. [12] studied free vibration characteristics of rotating axially functionally graded tapered beams by using the finite element method with basic displacement functions. Li and co-workers [13, 14] investigated dynamic characteristics of rotating FGM beams and FGM plates by using rigid-flexible coupled dynamics theory. Frequency veering and mode shift phenomena are discussed in their studies. Oh and Yoo [15] developed a structural model to study vibration characteristics of rotating pretwisted tapered blades made of FGMs.

Active piezoelectric actions of structures have been investigated extensively. Baz and Poh [16] studied the structural vibration control of flexible beams by using piezoelectric actuators via an effective modified independent modal space control (MIMSC) method. Liao and Wang [17] pointed out that a beneficial active-passive hybrid control system could be achieved by

setting up design guidelines to effectively integrate the host structure with the piezoelectric and viscoelastic materials. Li and Lyu [18] investigated the active vibration control of sandwich beams with pyramidal lattice core using the piezoelectric actuator/sensor pairs. Recently, Maruani et al. [19] studied the static and dynamic behaviors of a beam made of functionally graded piezoelectric material (FGPM) based on Timoshenko's hypothesis and layerwise approximation. Wang et al. [20] investigated the dynamic shape control of flexible wings by considering the interactions between structural dynamics, unsteady aerodynamics and piezo-actuators. Chai et al. [21] studied aerothermoelastic characteristics and active flutter control of composite laminated panels with time-dependent boundary conditions in supersonic airflow using MFC materials. Active vibration control studies on rotating beams by using piezoelectric materials are relatively fewer. Some researches were reported by Choi and Han [22], Sun and Mills [23], and Huang et al. [24]. The rotating beams considered by these authors are uniform and homogeneous, and there are also some researches focusing on rotating composite beams with piezoelectric materials [25-27]. Choi et al. [25] studied the bending vibration control of the pre-twisted rotating composite thin-walled beam with piezoelectric fiber composites. Wang et al. [26] studied the active control for vibration suppression of a rotating thin-walled beam theory incorporating fiber-reinforced and piezo-composite, and made explicit discussions for transverse shear force and twist moment actuators. Chandiramani [27] investigated the optimal control of a thin-walled rotating beam with piezoelectric sensor-actuator pairs. To the best of authors' knowledge, there is no correlative literature on the active vibration control of rotating FGM beams under thermal environment. One can only find some recent contributions on active vibration control of smart composite structures without large motions. Bodaghi et al. [28] studied the non-linear active control of dynamic responses of functionally graded beams in thermal environments exposed to blast loadings. Selim et al. [29] studied active vibration control of FGM plates with piezoelectric layers based on Reddy's higher-order shear deformation theory by using the element-free IMLS-Ritz method. In their work, effect of thermal environments was not discussed. Zhang et al. [30] studied the aeroelastic properties of functionally graded CNT-reinforced cylindrical shell in a supersonic airflow under thermal environments. Phung-Van and coauthors [31] performed extensive studies on static and free vibration analyses and dynamic control of composite plates with piezoelectric sensors and actuators by the cell-based smoothed discrete shear gap method (CS-FEM-DSG3). They proposed efficient computational approaches based on isogeometric analysis (IGA) [32, 33] and based on a generalized unconstrained approach in conjunction with IGA [34] for dynamic control of smart piezoelectric composite plates using higher-order shear deformation theory

(HSDT). Phung-Van et al. [35] developed an efficient computational approach based on the generalized shear deformation model and IGA for geometrically nonlinear transient analysis of piezoelectric functionally graded plates under thermo-electro-mechanical loadings. Aksencer and Aydogdu [36] reported that the attached point mass in rotating composites structures can be used to regulate the airflow in the wind turbine or to increase the flexibility in the car's fan and to change the vibration frequencies in the helicopter rotor.

The purpose of this paper is to propose a rigid-flexible coupled dynamic model for a rotating flexible beam made of FGMs with bonded piezoelectric films on the top and bottom surfaces of the beam and a lumped mass in thermal environment, and to examine the performance of the active vibration control of the smart system by using the proposed HOC model. To derive the equations of motion of the system, the HOC modeling theory introduced by Li et al. [13] is employed. The typical material properties of the FGM beam are assumed to be graded in the thickness direction. Based on the present dynamic model, the performance of the active control of the thermally induced vibration of the rotating FGM beam is evaluated and compared with the LOC model. The free vibration analysis of the rotating smart FGM beam system is also investigated.

## 2 Physical model and equations

In this paper, the rotating composite beam considered is very slender. The following assumptions are made for the analysis:

- 1) The FGM beam is a uniform Euler-Bernoulli beam; the two PZT layers bonded to the FGM beam are also treated as uniform Euler-Bernoulli beams. The Euler-Bernoulli beam theory disregards the transverse shear deformation and rotary inertia effects of the beam.
- 2) The FGM beam is made of ceramic and metal materials and its Young's modulus, density, thermal conductivity, and thermal expansion coefficient are assumed to follow a power law gradient distribution and vary in the thickness direction.
- 3) The Young's modulus and the thermal expansion coefficients of the FGM beam are temperature-dependent, while the other material properties are independent of the temperature.
- 4) The PZT layer with uniform voltage applied on it is polarized across the thickness direction.
- 5) The longitudinal shrinking caused by transverse deformation of the beam is included in the longitudinal deformation of each sub-layer beam and the transverse deformations of all the sub-layer beams are equal.
- 6) The FGM beam rotates in a horizontal plane and the gravity effect is neglected.

As shown in Fig. 1, the rotating FGM beam with two PZT layers bonded to its surface along the thickness direction of the beam is attached to the rigid hub of radius  $R$  and rotates about the center axis of the hub in a fixed planar coordinate system  $o_0x_0y_0$ . The rotation angle of the hub is  $\theta_0$ . A planar floating frame of reference that is tangent to the attachment point of the centroid line of the FGM beam to the hub and rotates with the FGM beam is denoted by  $o_1x_1y_1$ . The length and width of the FGM beam and the PZT layer are  $l$  and  $b$ , respectively. The thicknesses of the FGM beam and the PZT layer are  $h$  and  $h_p$ , respectively. The Young's modulus and mass density of the PZT material are  $E_p$  and  $\rho_p$ , respectively. The rotary inertia of the hub is  $J_{oh}$ , and  $\tau$  is the external torque on the hub. A lumped mass with mass  $m_l$  is on the FGM beam. The Cartesian coordinate of the lumped mass before deformation is  $(l, 0)$  in the  $o_1x_1y_1$  coordinate system.

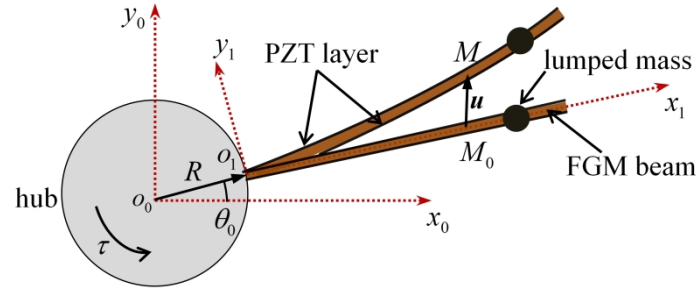


Fig. 1. Schematic of the rotating smart structure.

The FGM beam is designed as a thermal barrier structure made up of heat-resistant ceramics and tough metals, the top surface of the beam is ceramic rich and the bottom is metal rich. It is known that the effective material properties of the FGM beam can be estimated by Mori-Tanaka method, which is applicable to nanoparticles or the rule of mixture [33, 35, 37]. Since the rule of mixture is simple and convenient to apply for predicting the overall material properties and responses of the structures, the graded properties of the FGM beam is assumed to vary according to a power law distribution as

$$P(y) = P_m + (P_c - P_m)V_c \quad (1a)$$

$$V_c = \left( \frac{2y+h}{2h} \right)^N, \quad -\frac{h}{2} \leq y \leq \frac{h}{2} \quad (1b)$$

where  $y$  is coordinate in the thickness direction of the FGM beam;  $P(y)$  is effective material properties of the FGM and can be replaced by the Young's modulus  $E_f(y)$ , the mass

density  $\rho_f(y)$ , the thermal conductivity  $K_f(y)$ , or the thermal expansion coefficient  $\alpha_f(y)$ ; the subscripts 'c' and 'm' represent ceramic and metallic materials, respectively;  $V_c$  is volume fraction of metal;  $N$  is the volume fraction exponent. Fig. 2 shows the variation of the volume fraction function versus non-dimensional thickness  $y/h$  with different volume fraction exponent.

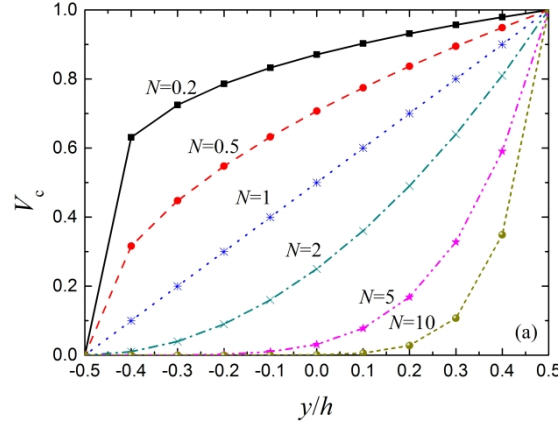


Fig. 2. Variation of the volume fraction function versus the non-dimensional thickness.

It is assumed that the variation of temperature occurs in the thickness direction of the FGM-PZT beam. The thermal analysis of the system is performed by solving a one-dimensional steady state heat transfer equation:

$$-\frac{d}{dy} \left[ K(y) \frac{dT(y)}{dy} \right] = 0 \quad (2)$$

where

$$K(y) = \begin{cases} K_p & (h/2 < y < h_p + h/2), \\ K_f(y) & (-h/2 \leq y \leq h/2), \\ K_p & (-h_p - h/2 < y < -h/2). \end{cases} \quad (3a)$$

$$T(y) = \begin{cases} T_p(y) & (h/2 < y < h_p + h/2), \\ T_f(y) & (-h/2 \leq y \leq h/2), \\ \tilde{T}_p(y) & (-h_p - h/2 < y < -h/2). \end{cases} \quad (3b)$$

where  $K_p$  is the thermal conductivity of the PZT layers;  $K(y)$  is the thermal conductivity of the FGM-PZT beam;  $T_p(y)$ ,  $\tilde{T}_p(y)$ , and  $T_f(y)$  are the temperature gradient fields of the upper PZT layer, the lower PZT layer, and the FGM beam, respectively. The thermal Dirichlet

boundary conditions and the continuity conditions are as follows [4]:

$$T_p(h_p + h/2) = T_U, \quad \tilde{T}_p(-h_p - h/2) = T_L \quad (4a)$$

$$T_p(h/2) = T_f(h/2) = T_c, \quad T_f(-h/2) = \tilde{T}_p(-h/2) = T_m \quad (4b)$$

$$K_p \frac{dT_p(y)}{dy} \Big|_{y=h/2} = K_c \frac{dT_f(y)}{dy} \Big|_{y=h/2}, \quad K_p \frac{d\tilde{T}_p(y)}{dy} \Big|_{y=-h/2} = K_m \frac{dT_f(y)}{dy} \Big|_{y=-h/2} \quad (4c)$$

where  $T_U$  and  $T_L$  are temperatures of the upper and lower surfaces of the FGM-PZT beam, respectively;  $T_c$  and  $T_m$  are temperatures of the ceramic-rich and metal-rich surfaces of the FGM beam and can be expressed by

$$T_c = T_m + (T_U - T_L) - \frac{K_c D + K_m}{K_m} (T_m - T_L), \quad T_m = T_L + \frac{\frac{K_m}{Ch} (T_U - T_L)}{\frac{K_p}{h_p} + \frac{K_c D + K_m}{Ch}} \quad (5)$$

in which

$$C = 1 - \frac{K_{cm}}{(N+1)K_m} + \frac{K_{cm}^2}{(2N+1)K_m^2} - \frac{K_{cm}^3}{(3N+1)K_m^3} + \frac{K_{cm}^4}{(4N+1)K_m^4} - \frac{K_{cm}^5}{(5N+1)K_m^5} \quad (6a)$$

$$D = 1 - \frac{K_{cm}}{K_m} + \left(\frac{K_{cm}}{K_m}\right)^2 - \left(\frac{K_{cm}}{K_m}\right)^3 + \left(\frac{K_{cm}}{K_m}\right)^4 - \left(\frac{K_{cm}}{K_m}\right)^5 \quad (6b)$$

The solution of Eq. (2) is obtained by means of polynomial series [38]:

$$T_p(y) = T_c + \frac{T_U - T_c}{h_p} (y - h/2) \quad (7a)$$

$$\tilde{T}_p(y) = T_L + \frac{T_m - T_L}{h_p} (y + h/2 + h_p) \quad (7b)$$

$$\begin{aligned} T_f(y) = T_m + \frac{T_c - T_m}{C} & \left[ \left( \frac{2y+h}{2h} \right) - \frac{K_{cm}}{(N+1)K_m} \left( \frac{2y+h}{2h} \right)^{N+1} + \frac{K_{cm}^2}{(2N+1)K_m^2} \left( \frac{2y+h}{2h} \right)^{2N+1} \right. \\ & - \frac{K_{cm}^3}{(3N+1)K_m^3} \left( \frac{2y+h}{2h} \right)^{3N+1} + \frac{K_{cm}^4}{(4N+1)K_m^4} \left( \frac{2y+h}{2h} \right)^{4N+1} \\ & \left. - \frac{K_{cm}^5}{(5N+1)K_m^5} \left( \frac{2y+h}{2h} \right)^{5N+1} \right] \quad (7c) \end{aligned}$$

with

$$T_{cm} = T_c - T_m, \quad K_{cm} = K_c - K_m \quad (8)$$

Temperature-dependency of the Young's modulus and the thermal expansion coefficients of the FGM beam can be expressed as nonlinear functions of temperature [39]:

$$P = P_0 \left( P_{-1}/T + 1 + P_1 T + P_2 T^2 + P_3 T^3 \right) \quad (9)$$

where  $P_0$ ,  $P_{-1}$ ,  $P_1$ ,  $P_2$  and  $P_3$  are constants in the cubic fit of the material properties.

An arbitrary point  $M_0$  on the FGM beam moves to the point  $M$  in Fig. 1. The position vector of the point  $M$  in the  $o_1x_1y_1$  coordinate system is expressed by

$$\mathbf{r} = \left( R + x + w_1 + w_c - y \left( \frac{\partial w_2}{\partial x} \right) \right) \mathbf{x} + w_2 \mathbf{y} \quad (10)$$

where  $w_1$  is the deformation of the beam along its axial direction, and  $w_c = -(1/2) \int_0^x ((\partial w_2(\xi, t)/\partial \xi))^2 d\xi$  is a second-order coupling term that represents longitudinal shrinking of the beam caused by the transverse displacement [13];  $w_2$  is the transverse displacement of the point  $M$ .

The position vector of an arbitrary point on the centroid line of the top and the bottom piezoelectric layers can be written as

$$\mathbf{r}_{p1} = \left[ R + x + w_1 + w_c - \frac{h + h_p}{2} \left( \frac{\partial w_2}{\partial x} \right) \right] \mathbf{x} + w_2 \mathbf{y} \quad (11a)$$

and

$$\mathbf{r}_{p2} = \left[ R + x + w_1 + w_c + \frac{h + h_p}{2} \left( \frac{\partial w_2}{\partial x} \right) \right] \mathbf{x} + w_2 \mathbf{y} \quad (11b)$$

, respectively.

The position vector of the lumped mass after deformation can be written as

$$\mathbf{r}_l = (R + l_1 + w_1(l_1, t) + w_c(l_1, t)) \mathbf{x} + w_2(l_1, t) \mathbf{y} \quad (12)$$

Differentiating Eqs. (10)-(12) with respect to time yields

$$\begin{cases} \dot{\mathbf{r}} = \left( \dot{w}_1 + \dot{w}_c - w_2 \dot{\theta}_0 - y \left( \frac{\partial^2 w_2}{\partial x \partial t} \right) \right) \mathbf{x} + \left[ \left( R + x + w_1 + w_c - y \left( \frac{\partial w_2}{\partial x} \right) \right) \theta_0 + \dot{w}_2 \right] \mathbf{y} \\ \dot{\mathbf{r}}_{p1} = \left( \dot{w}_1 + \dot{w}_c - \frac{h+h_p}{2} \left( \frac{\partial^2 w_2}{\partial x \partial t} \right) - w_2 \dot{\theta}_0 \right) \mathbf{x} + \left[ \left( R + x + w_1 + w_c - \frac{h+h_p}{2} \left( \frac{\partial w_2}{\partial x} \right) \right) \theta_0 + \dot{w}_2 \right] \mathbf{y} \\ \dot{\mathbf{r}}_{p2} = \left( \dot{w}_1 + \dot{w}_c + \frac{h+h_p}{2} \left( \frac{\partial^2 w_2}{\partial x \partial t} \right) - w_2 \dot{\theta}_0 \right) \mathbf{x} + \left[ \left( R + x + w_1 + w_c + \frac{h+h_p}{2} \left( \frac{\partial w_2}{\partial x} \right) \right) \theta_0 + \dot{w}_2 \right] \mathbf{y} \\ \dot{\mathbf{r}}_i = \left( \dot{w}_1(l_i, t) + \dot{w}_c(l_i, t) - w_2(l_i, t) \dot{\theta}_0 \right) \mathbf{x} + \left[ \left( R + l_i + w_1(l_i, t) + w_c(l_i, t) \right) \theta_0 + \dot{w}_2(l_i, t) \right] \mathbf{y} \end{cases} \quad (13)$$

where an overdot denotes a time derivative. The kinetic energy of the system is

$$T = \frac{1}{2} J_{oh} \dot{\theta}_0^2 + \frac{1}{2} \int_{V_f} \rho(y) \dot{\mathbf{r}}^T \dot{\mathbf{r}} dV_f + \frac{1}{2} \int_{V_p} \rho_p \dot{\mathbf{r}}_{p1}^T \dot{\mathbf{r}}_{p1} dV_p + \frac{1}{2} \int_{V_p} \rho_p \dot{\mathbf{r}}_{p2}^T \dot{\mathbf{r}}_{p2} dV_p + \frac{1}{2} m_i \dot{\mathbf{r}}_i^T \dot{\mathbf{r}}_i \quad (14)$$

in which  $V_f$  and  $V_p$  are the volumes of the FGM beam and piezoelectric layers, respectively.

The longitudinal normal strain of the beam at the point  $M_0$  is expressed as

$$\varepsilon_x = \frac{\partial w_1}{\partial x} - y \frac{\partial^2 w_2}{\partial x^2} \quad (15)$$

The potential energy of the system can be written as

$$V = \frac{1}{2} \int_{V_f} E(y) \varepsilon_x^2 dV_f + \int_{V_p} E_p \varepsilon_x^2 dV_p \quad (16)$$

By the method of assumed modes,  $w_1$  and  $w_2$  can be expressed by

$$\begin{cases} w_1 = \Phi_x(x) \mathbf{A}(t) \\ w_2 = \Phi_y(x) \mathbf{B}(t) \end{cases} \quad (17)$$

where  $\Phi_x(x) \in \mathbf{R}^{1 \times K}$  and  $\Phi_y(x) \in \mathbf{R}^{1 \times K}$  are vectors of trial functions associated with the longitudinal and transverse vibrations of the FGM beam, respectively;  $\mathbf{A}(t) \in \mathbf{R}^{K \times 1}$  and  $\mathbf{B}(t) \in \mathbf{R}^{K \times 1}$  are generalized coordinate vectors associated with the longitudinal and transverse vibrations of the FGM beam, respectively. Substituting Eq. (17) into the expression  $w_c$  yields

$$w_c = -\frac{1}{2} \mathbf{B}^T \mathbf{H}(x) \mathbf{B} \quad (18)$$

where

$$\mathbf{H}(x) = \int_0^x \Phi_y'^T(\xi) \Phi_y'(\xi) d\xi \quad (19)$$

in which a prime denotes a derivative with respect to the argument.

Let  $\mathbf{q} = (\theta_0 \mathbf{A}^T \mathbf{B}^T)^T$  be the global generalized coordinate vector, the virtual work done by the external driving torque  $\tau$  is

$$\delta W_\tau = \mathbf{Q}_\tau^T \delta \mathbf{q} \quad (20)$$

where  $\mathbf{Q}_\tau = (\tau \mathbf{0} \mathbf{0})^T$  is the generalized external forces associated with the torque.

The virtual work done by the piezoelectric force that caused by the induced strain  $\varepsilon_p$  in the piezoelectric layer is given by [40]

$$\delta W_p = \mathbf{Q}_p \delta \mathbf{q} = E_p A_p \int_0^l \left( \varepsilon_p \delta w_1 + d_0 \varepsilon_p \delta \left( \frac{\partial w_2}{\partial x} \right) \right) dx \quad (21)$$

with

$$\varepsilon_p = d_{31} \phi_c / h_p \quad (22)$$

$$d_0 = h + h_p \quad (23)$$

where  $\mathbf{Q}_p$  is the generalized force associated with the piezo-electric force;  $A_p = bh$  is the cross-sectional area of the piezoelectric layer;  $d_{31}$  is the piezoelectric strain constant;  $\phi_c$  is the actuator voltage across the piezoelectric layer and it is generated by applying a proportional and derivative control law [41]:

$$\phi_c = -K_p \phi_s - K_d d\phi_s / dt \quad (24)$$

where  $K_p$  and  $K_d$  are the proportional and derivative control gains, respectively;  $\phi_s$  is the piezo-sensor voltage, which is given by

$$\phi_s = -\frac{k_{31}^2 D_d b}{g_{31} C} \int_0^l \left( \frac{\partial^2 w_2}{\partial x^2} \right) dx \quad (25)$$

with

$$D_d = h/2 \quad (26)$$

$$C = 8.854 \times 10^{-12} b l k_{31} / h \quad (27)$$

where  $k_{31}$  is the electro-mechanical coupling factor,  $g_{31}$  is the piezo-electric voltage constant,  $D_d$  is the distance from the beam neutral axis to the piezo-sensor surface,  $k_{31}$  is the dielectric constant and  $C$  is the capacitance of the sensor. The generalized force associated with the piezo-electric force can be written as

$$\mathbf{Q}_p = (0 \mathbf{Q}_{pf} \mathbf{Q}_{pm})^T \quad (28)$$

in which

$$\mathbf{Q}_{pf} = g(K_p + K_d p) \int_0^l \Phi_x'^T \left( \int_0^l \Phi_y'' B dx \right) dx \quad (29)$$

$$\mathbf{Q}_{pm} = d_0 g(K_p + K_d p) \int_0^l \Phi_y''^T \left( \int_0^l \Phi_y'' B dx \right) dx \quad (30)$$

with

$$p = \frac{d}{dt} \quad (31)$$

$$g = E_p b^2 d_{31} k_{31}^2 D_d / g_{31} C \quad (32)$$

The virtual work done by the temperature load is given as

$$\delta W_T = \int_V \delta \varepsilon_x \sigma_T dV = \int_V \delta \varepsilon_x E(y, T) (-\alpha(y, T) \Delta T) dV = \mathbf{Q}_T^T \delta \mathbf{q} \quad (33)$$

where  $\Delta T = T - T_0$ ,  $T_0$  is the reference temperature,  $\mathbf{Q}_T$  is the generalized force associated with the temperature load that can be written as

$$\mathbf{Q}_T = [0, \mathbf{Q}_{T1}, \mathbf{Q}_{T2}]^T \quad (34)$$

in which

$$\mathbf{Q}_{T1} = \int_{-h_p - h/2}^{h_p + h/2} E(y) b \alpha(y) [T(y) - T_0] dy \int_0^l \Phi_x' dx \quad (35)$$

$$\mathbf{Q}_{T2} = - \int_{-h_p - h/2}^{h_p + h/2} y E(y) b \alpha(y) [T(y) - T_0] dy \int_0^l \Phi_y'' dx \quad (36)$$

The generalized force vector of the system that composes of the generalized external force  $\mathbf{Q}_r$ , the piezo-electric force  $\mathbf{Q}_p$ , and the temperature force  $\mathbf{Q}_T$  is given by

$$\mathbf{Q} = \mathbf{Q}_r + \mathbf{Q}_p + \mathbf{Q}_T \quad (37)$$

Substituting Eq. (17) into Eq. (13) and Eq. (15), the discretized kinetic energy and potential energy of the system can be obtained from Eq. (14) and Eq. (16), respectively. Use Lagrange's equations:

$$\frac{d}{dt} \left( \frac{\partial T}{\partial \dot{\mathbf{q}}} \right) - \frac{\partial T}{\partial \mathbf{q}} = - \frac{\partial V}{\partial \mathbf{q}} + \mathbf{Q} \quad (38)$$

yields

$$\begin{bmatrix} M_{11} & M_{12} & M_{13} \\ M_{21} & M_{22} & M_{23} \\ M_{31} & M_{32} & M_{33} \end{bmatrix} \begin{bmatrix} \ddot{\theta}_0 \\ \ddot{A} \\ \ddot{B} \end{bmatrix} = \begin{bmatrix} Q_{\theta_0} \\ Q_A \\ Q_B \end{bmatrix} \quad (39)$$

Eq. (39) provides a high order rigid-flexible coupled (HOC) dynamic model of the rotating

hub-smart beam structure in variable gradient temperature environment. The matrices in Eq. (39) are given in detail in Appendix A. It should be mentioned that, the double underlined terms appeared in the matrices in Appendix A, resulting from the second-order coupling term  $w_c$ , are retained in this paper. Note that by removing these high order nonlinear terms and keeping the single underlined terms associated with  $w_c$ , Eq. (39) will degrade into a traditional low order coupled (LOC) model [13]. The piezoelectric effect and thermal effect are both considered in the dynamic equations of the system, which model is also a high-order electro-thermal-mechanical coupling dynamic model.

Assume that the angular velocity of the rotating hub  $\dot{\theta}_0 = \Omega$  is constant; hence  $\ddot{\theta}_0 = 0$ . Using the second and third equations in Eq. (39), one can obtain the linearized coupled longitudinal stretching and chordwise bending vibration equations of the system:

$$\begin{bmatrix} \underline{M}_x & \underline{0} \\ \underline{0} & \underline{M}_y \end{bmatrix} \begin{bmatrix} \underline{\ddot{A}} \\ \underline{\ddot{B}} \end{bmatrix} + \begin{bmatrix} \underline{0} & \underline{G}_{23} \\ \underline{G}_{32} & \underline{G}_{33} \end{bmatrix} \begin{bmatrix} \underline{\dot{A}} \\ \underline{\dot{B}} \end{bmatrix} + \begin{bmatrix} \underline{K}_{22} & \underline{K}_{23} \\ \underline{K}_{32} & \underline{K}_{33} \end{bmatrix} \begin{bmatrix} \underline{A} \\ \underline{B} \end{bmatrix} = \underline{0} \quad (40)$$

where the detailed expressions of the matrices are given in Appendix B.

Eq. (40) can be written in the first-order form:

$$\underline{M}\dot{\underline{z}} + \underline{K}\underline{z} = \underline{0} \quad (41)$$

where

$$\underline{z} = \begin{bmatrix} \underline{\dot{A}} \\ \underline{\dot{B}} \\ \underline{A} \\ \underline{B} \end{bmatrix}, \quad \underline{M} = \begin{bmatrix} \underline{M}_x & \underline{0} & \underline{0} & \underline{0} \\ \underline{0} & \underline{M}_y & \underline{0} & \underline{0} \\ \underline{0} & \underline{0} & \underline{I} & \underline{0} \\ \underline{0} & \underline{0} & \underline{0} & \underline{I} \end{bmatrix}, \quad \underline{K} = \begin{bmatrix} \underline{0} & \underline{G}_{23} & \underline{K}_{22} & \underline{K}_{23} \\ \underline{G}_{32} & \underline{G}_{33} & \underline{K}_{32} & \underline{K}_{33} \\ \underline{-I} & \underline{0} & \underline{0} & \underline{0} \\ \underline{0} & \underline{-I} & \underline{0} & \underline{0} \end{bmatrix} \quad (42)$$

The eigenvalue problem associated with Eq. (41) is

$$(\lambda_j \underline{M} + \underline{K})\underline{Z} = \underline{0} \quad (43)$$

where  $\lambda_j = \sigma_j + i\omega_j$  is the  $j$ th complex eigenvalue,  $\underline{Z}$  is the  $j$ th eigenvector;  $\sigma_j$  represents the vibration exponential decay,  $\omega_j$  is the damped frequency. The damping ratio is given by

$$\xi_j = -\frac{\sigma_j}{\sqrt{\sigma_j^2 + \omega_j^2}} \quad (44)$$

### 3 Vibration control and analysis

#### 3.1 Comparison studies

For validation purpose, natural frequencies of a non-rotating FG beam with or without the

temperature effect are first studied and compared with those available in literature. Azadi [42] developed a finite element method for free and forced lateral vibration analysis of beams made of FGMs whose material properties were temperature dependent and graded in the thickness direction according to the power law distribution of the volume fractions of the constituents. In his work, only the effective Young's modulus depends to temperature. Following the same assumption of Azadi's work, the thermal expansion coefficients of the FGM beam is temperature independent. The dynamic equations can be obtained from the model developed in section 2 by removing the PZT layers. Table 1 shows the comparison of the first four chordwise bending natural frequencies of a metal-rich FG beam ( $N=0$ ) calculated from the present method to the analytical solutions and to those reported in Ref. [42]. Two different boundary conditions (CF: clamped-free, SS: simply supported) are considered. The properties and geometrical characteristics of the FGM beam are the same as those in Ref. [42]. As they can be seen from the table, the results from the proposed method agree quite well with those from literature. Table 2 compares the first four chordwise bending natural frequencies of a simply-supported FG beam ( $N=1$ ) for various temperatures calculated from the present method to those reported in Ref. [42]. The results obtained from the present method agree very well with those from Ref. [42].

To further validate the present method, vibration of a similar flexible smart beam with a tip mass in Ref. [24] is investigated. The model of the system using finite element method in Ref. [24] is used for validation. We now ignore the temperature-dependency effect of material properties, and let the lumped mass be located at the tip of the nonrotating flexible beam with  $N=0$ . Basic parameters of the system with piezoelectric layer in close loop and tip mass (Structure B in Ref. [24]) are given as follows:  $R=0$  m,  $l=8$  m,  $b=1.985\times 10^{-3}$  m,  $h=3.6765\times 10^{-2}$  m,  $h_p=2.667\times 10^{-4}$  m,  $E_b=68.952$  Gpa,  $\rho_b=2766.7$  kg/m<sup>3</sup>,  $E_p=139$  Gpa,  $\rho_p=7500$  kg/m<sup>3</sup>,  $m_l=0.085$  kg. The piezoelectric coefficients used here are also consistent with those given in Ref. [24]. Table 3 shows the first six frequencies of the system obtained from the present method and the method in Ref. [24]. Again, the present results match quite well with those in literature. Thus, the accuracy of the present dynamic model is validated and it can be further applied to the dynamics and control of a rotating FGM-PZT beam in temperature field.

Table 1 Chordwise bending natural frequencies of metal-rich FG beam,  $N = 0$ . (unit: Hz)

Mode Number	Clamped-free			Simply-supported		
	Analytical	Ref. [42]	Present	Analytical	Ref. [42]	Present
1	144.0	144.1	144.0	404.3	404.1	404.3
2	902.7	902.3	902.7	1617.4	1617.1	1617.4
3	2527.6	2527.0	2527.6	3639.1	3639.0	3639.1
4	4953.1	4951.5	4953.1	6469.4	6469.5	6469.4

Table 2 Chordwise bending natural frequencies if SS FG beam for different temperature,  $N = 1$ . (unit: Hz)

Mode Number	$T = 350$ (K)		$T = 400$ (K)		$T = 450$ (K)		$T = 500$ (K)	
	Ref. [42]	Present						
1	487.0	487.1	482.8	482.9	478.7	478.8	474.7	474.8
2	1948.1	1948.3	1931.4	1931.7	1914.9	1915.0	1898.7	1898.9
3	4383.3	4383.4	4345.6	4345.8	4308.6	4308.7	4272.2	4272.3
4	7792.5	7792.5	7725.5	7725.4	7659.7	7659.6	7594.9	7594.8

Table 3 The first six frequencies of the smart beam with tip mass. (unit: Hz)

	1st order	2nd order	3rd order	4th order	5th order	6th order
Ref. [24]	0.4564	2.8925	8.1539	16.0570	26.6574	40.0155
Present	0.4561	2.8922	8.1535	16.0561	26.6570	40.0151

### 3.2 Vibration control of the system when a driving torque is applied on the hub

In this section, vibration control of the rotating FGM-PZT beam system in temperature field is studied by using the HOC model proposed in section 2. Temperature-dependent material properties for the FGM beam made of ceramic ( $\text{Si}_3\text{N}_4$ )/metal (Ti-6Al-4V) constituents from Ref. [39] are given in Table 4. The mass densities of  $\text{Si}_3\text{N}_4$  and Ti-6Al-4V are  $4429 \text{ kg/m}^3$  and  $2370 \text{ kg/m}^3$ , respectively. The thermal conductivities of  $\text{Si}_3\text{N}_4$  and Ti-6Al-4V are  $9.19 \text{ W/mk}$  and  $7.955 \text{ W/mk}$ , respectively. The geometrical properties of the FGM beam and PZT layers are as follows:  $l = 5 \text{ m}$ ,  $b = 0.02 \text{ m}$ ,  $h = 0.02 \text{ m}$ ,  $h_p = 0.002 \text{ m}$ . The material properties for the PZT are  $E_p = 63 \text{ Gpa}$ ,  $\rho_p = 7600 \text{ kg/m}^3$ ,  $K_p = 2.1 \text{ W/mk}$ ,  $\alpha_p = 0.9 \times 10^{-6}$ ,  $d_{31} = 23 \times 10^{-12} \text{ m/V}$ ,  $k_{31} = 0.12$ ,  $g_{31} = 216 \times 10^{-3} \text{ Vm/N}$ . The FGM-PZT beam rotates in a horizontal plane and the driving torque acting on the hub is  $\tau = 5 \exp(-120t)$ . The hub radius is  $R = 0.1 \text{ m}$  and the rotary inertia of the hub is  $J_{\text{oh}} = 0.0015 \text{ kg/m}^2$ . The mass of the lumped mass is  $m_l = 0.1 \text{ kg}$ .

Table 4 Temperature-dependent coefficients for ceramic and metal [39].

Materials	Properties	$P_0$	$P_{-1}$	$P_1$	$P_2$	$P_3$
Si <sub>3</sub> N <sub>4</sub>	$E_c$ (Pa)	348.43e+9	0	-3.070e-4	2.160e-7	-8.964e-11
	$\alpha_c$ (1/K)	5.8723e-6	0	9.095e-4	0	0
Ti-6Al-4V	$E_m$ (Pa)	122.56e+9	0	-4.586e-4	0	0
	$\alpha_m$ (1/K)	7.5788e-6	0	6.638e-4	-3.147e-6	0

A FGM beam with volume fraction exponent  $N = 1$  is considered first. The lumped mass is located at the end of the FGM beam. Figs. 3(a)-(c) show the time histories of the rotating angle of the hub, the tip longitudinal deformation of the FGM beam, and the tip transverse deformation of the FGM beam in different temperature fields. The reference temperature is  $T_0 = 273.15$  K. When the temperature gradient field is considered in the rotating FGM-PZT beam system, the temperature difference between the upper and lower surfaces of the FGM-PZT beam is assumed to be  $\Delta T = 0$  K, 50 K, 100K, respectively. There is no control piezoelectric force acting on the FGM beam and the proportional and derivative control gains are  $K_p = K_d = 0$ . As it can be seen from the figures, the thermal flutter phenomena can be observed and the amplitudes of the dynamic responses of the system increase obviously after the temperature gradient field is applied. It is clear that the thermally induced vibration has adverse effects on the system and should be suppressed. Note that the value of the rotating angle of the hub is quite small (less than 0.1 rad, see Fig. 3a). It is reasonable to assume that the temperature difference exists between the upper and lower surfaces of the composite beam, which is a similar case of a non-rotating beam exposing in temperature environments with temperature gradient.

Figs. 4(a)-(b) show the time histories of the rotating angle and the angular velocity of the hub with and without control, respectively. The temperature difference is  $\Delta T = 50$  K. The control gains are selected as  $K_p = 1$  and  $K_d = -10$ . One can see from Fig. 4(a) that the flutter amplitude of the angular displacement response of the hub is greatly decreased after the piezoelectric active control works. The angular velocity of the hub reduces to zero quickly when the system is under control, as it can be seen from Fig. 4(b).

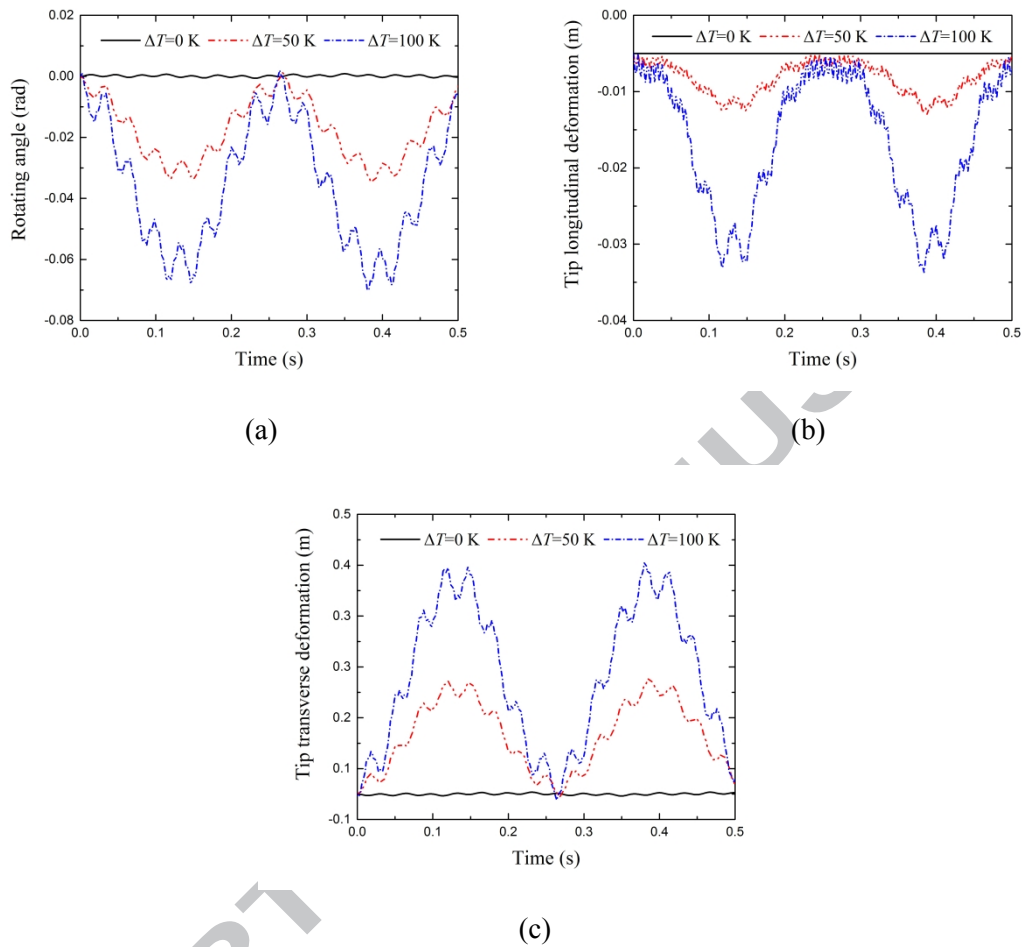


Fig. 3. The time histories of (a) the rotating angle of the hub, (b) the tip longitudinal deformation and (c) the tip transverse deformation of the FGM beam in different temperature fields.

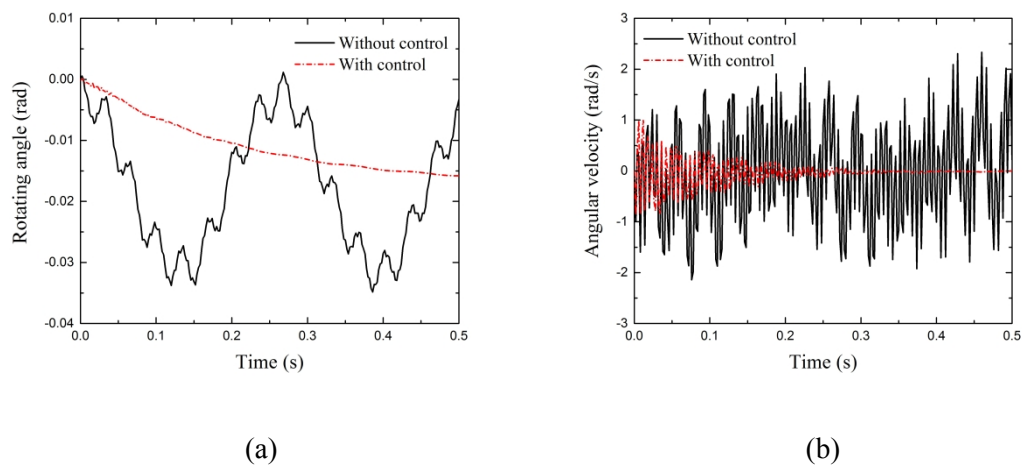


Fig. 4. The time histories of (a) the rotating angle and (b) the angular velocity of the hub with

and without control.

Figs. 5(a)-(b) show the time histories of the tip longitudinal deformation and the tip longitudinal velocity of the FGM beam with and without control. Figs. 6(a)-(b) show the time histories of the tip transverse deformation and the tip transverse velocity of the FGM beam with and without control. The thermally induced vibrations of the FGM beam along the longitudinal and transverse directions are quickly suppressed under the active control. The flutter velocities of the FGM beam along the longitudinal and transverse directions reduce to zero at about the same time. Fig. 7 shows the time histories of the voltage applied on the FGM when  $K_d$  is selected as -10, -20, -50, and -100, respectively. It is interesting to see that as the absolute value of  $K_d$  becomes larger, the needed feedback control voltage becomes smaller. The cost of the smart vibration control can be reduced by properly selecting the control gain.

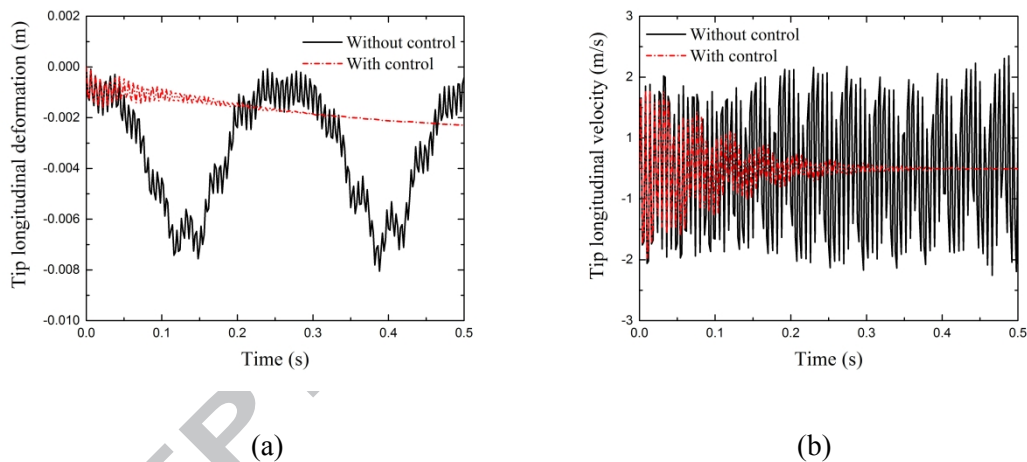


Fig. 5. The time histories of (a) the tip longitudinal deformation and (b) the tip longitudinal velocity of the FGM beam with and without control.

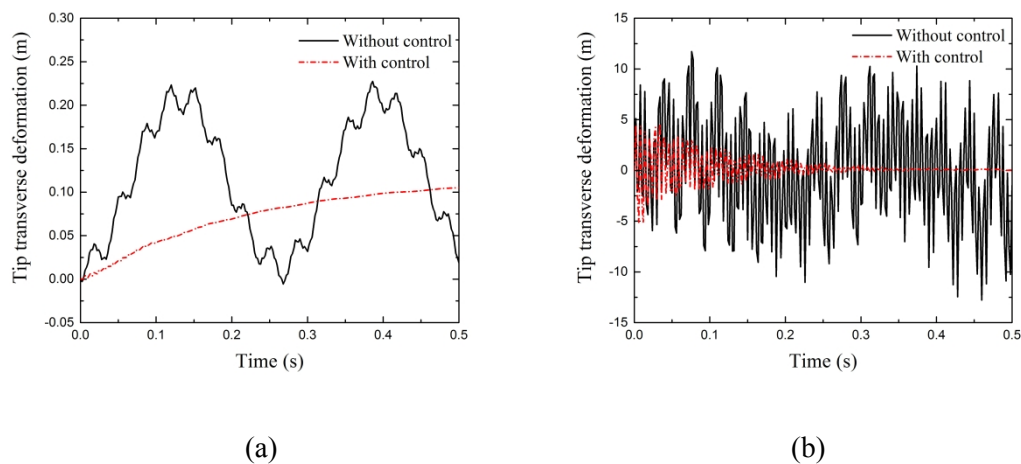


Fig. 6. The time histories of (a) the tip transverse deformation and (b) the tip transverse

velocity of the FGM beam with and without control.

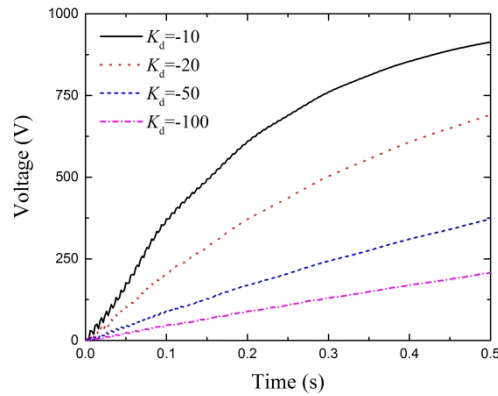


Fig. 7. The time histories of the voltage applied on the FGM beam with different  $K_d$ .

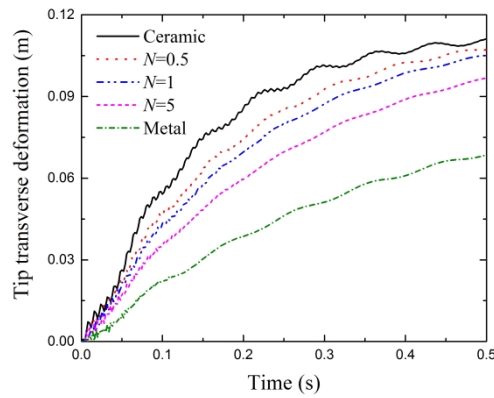


Fig. 8. Influence of the material volume fraction exponent on transverse deformation of the FGM-PZT beam.

Fig. 8 shows the time-history of the tip transverse deformation of the FGM-PZT beam under the temperature gradient  $\Delta T = 50$  K for various values of the volume fraction exponent  $N$  when the values of control gain are chosen as  $K_p = 1$  and  $K_d = -10$ . As it can be seen from this figure, the tip transverse deformation of the beam decreases when  $N$  increase from 0 (ceramic beam) to infinity (metal beam) due to the decrease in the stiffness of the FGM beam.

Figs. 9-13 show the time-histories of the tip dynamic responses of the FGM-PZT beam obtained from the LOC model and the present HOC model in different temperature gradients with  $N = 1$  when the values of control gain are chosen as  $K_p = 1$  and  $K_d = -10$ . The temperature gradients are assumed as  $\Delta T = 0$  K (Figs. 9(a)-(d)),  $\Delta T = 20$  K (Figs. 10(a)-(d)),  $\Delta T = 50$  K (Figs. 11(a)-(d)),  $\Delta T = 100$  K (Figs. 12(a)-(d)) and  $\Delta T = 200$  K (Figs. 13(a)-(d)), respectively. As they can be seen from Figs. 8(a)-(d), the dynamic responses of the smart beam calculated from the present HOC model are consistent with those from the LOC model when

there is no temperature gradient ( $\Delta T = 0$  K). However, Figs. 10-13 show that there are significant differences between the results from the HOC model and the LOC model when the temperature gradient increases. As shown in Figs. 10(a)-(d), when  $\Delta T = 20$  K, the differences of the tip transverse deformation and velocity of the beam obtained from the HOC model and the LOC model are relatively slight, while the differences of the tip longitudinal deformation and velocity of the beam obtained from the two models are quite obvious. In Figs. 11(a)-(b), when  $\Delta T = 50$  K, the differences of the tip longitudinal and transverse dynamic responses obtained from the HOC model and the LOC model are significant. Such differences are more pronounced as the values of  $\Delta T$  become larger. Due to the loss of the high order nonlinear terms, the dynamic responses calculated by the LOC model start to diverge in some cases and could not reflect the reality of the system under control. The HOC model, with the high order geometric nonlinearity included, captures physical behaviors better than the LOC model. It is indicated that the influence of high-order nonlinearity in the present HOC model on the characteristics of dynamics and control of flexible structures should not be ignored.

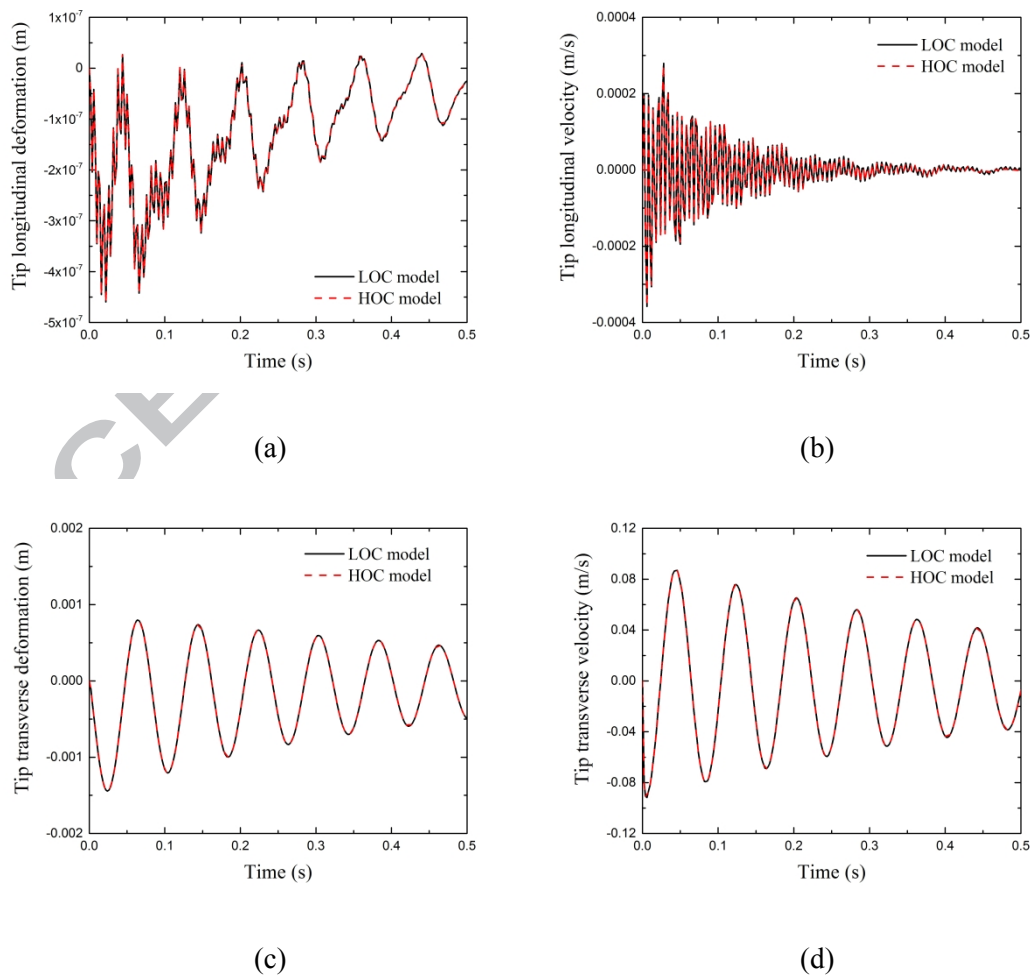


Fig. 9. Comparison of the tip dynamic responses of the FGM beam obtained from the LOC

model and the present HOC model with  $\Delta T = 0 \text{ K}$  ( $N = 1, K_p = 1, K_d = -10$ ).

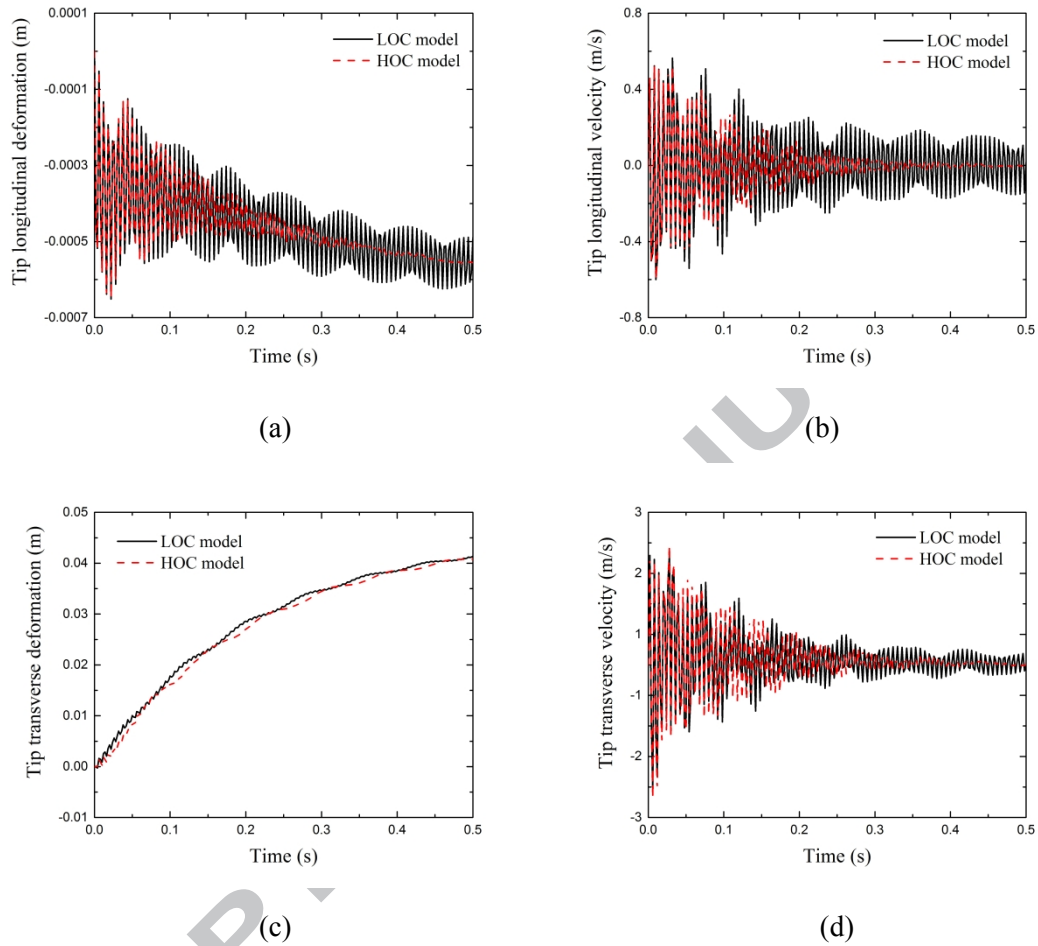
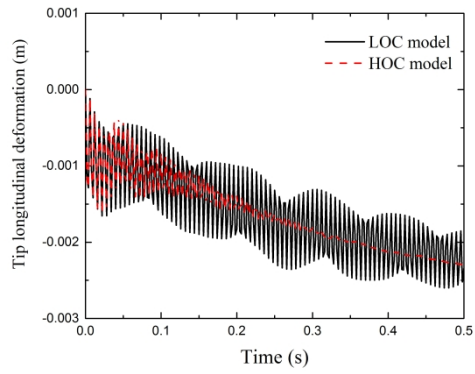
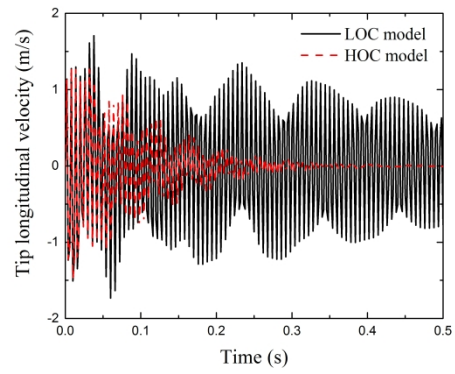


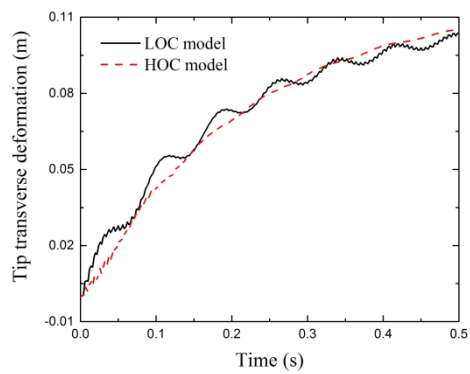
Fig. 10. Comparison of the tip dynamic responses of the FGM beam obtained from the LOC model and the present HOC model with  $\Delta T = 20 \text{ K}$  ( $N = 1, K_p = 1, K_d = -10$ ).



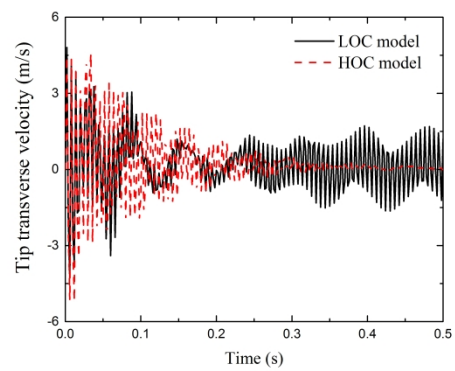
(a)



(b)



(c)



(d)

Fig. 11. Comparison of the tip dynamic responses of the FGM beam obtained from the LOC model and the present HOC model with  $\Delta T = 50$  K ( $N = 1$ ,  $K_p = 1$ ,  $K_d = -10$ ).

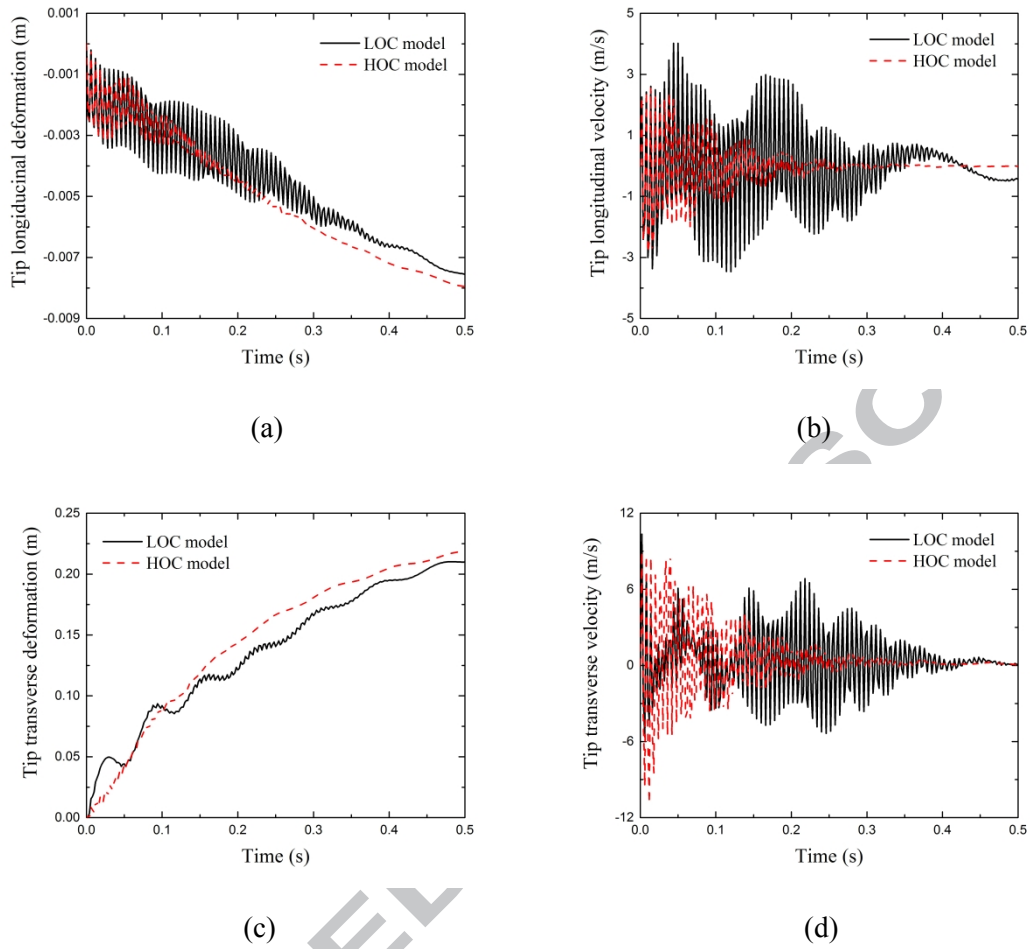


Fig. 12. Comparison of the tip dynamic responses of the FGM beam obtained from the LOC model and the present HOC model with  $\Delta T = 100 \text{ K}$  ( $N = 1, K_p = 1, K_d = -10$ ).

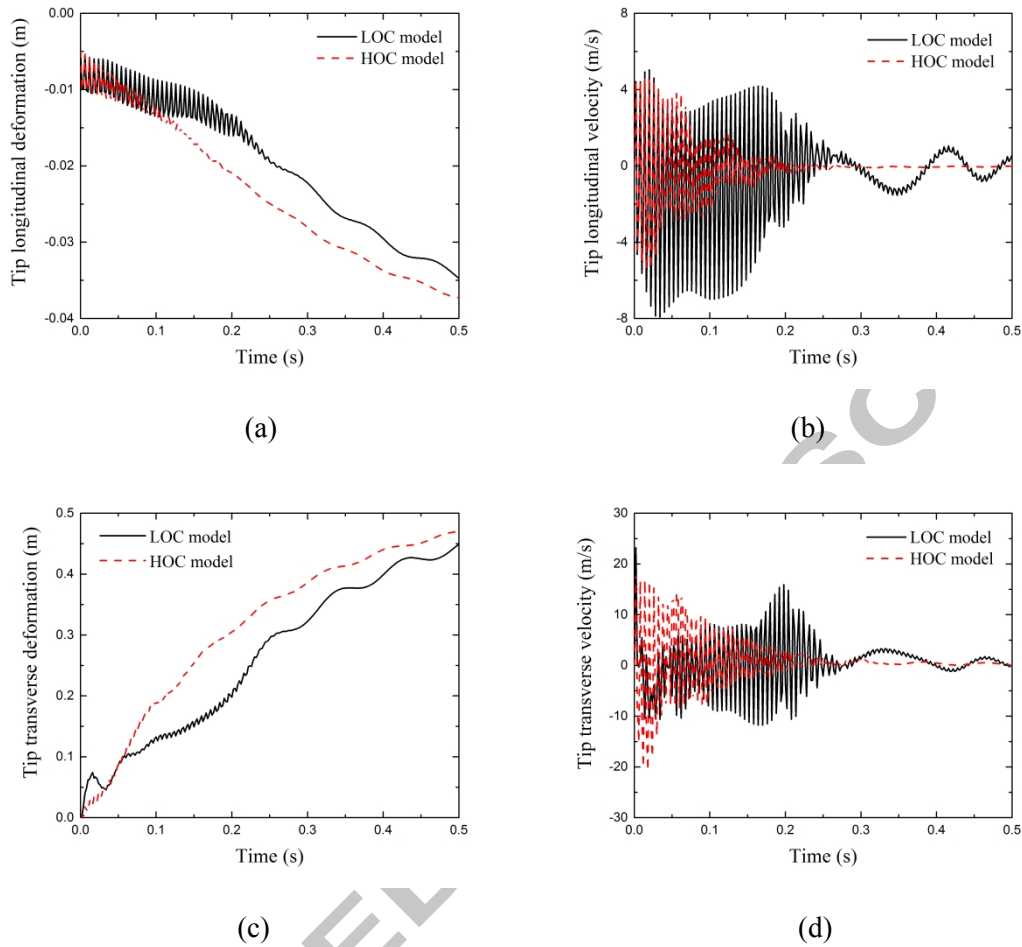


Fig. 13. Comparison of the tip dynamic responses of the FGM beam obtained from the LOC model and the present HOC model with  $\Delta T = 200$  K ( $N = 1, K_p = 1, K_d = -10$ ).

### 3.3 Free vibration analysis of the rotating smart FGM beam system

In this section, free vibration analysis of the FGM-PZT beam rotating at constant angular velocity is studied. The system parameters and material properties in section 3.1 are still used to perform the following simulations by using Eq. (40). Table 5 shows effect of the volume fraction exponent  $N$  and location of the lumped mass on the first natural frequency of the rotating FGM-PZT beam when  $\Omega = 200$  rpm in the ambient temperature field ( $T = 300$  K). The proportional and derivative control gains are selected as  $K_p = K_d = 0$ . The first natural frequency decreases when the volume fraction exponent is increased. This is because the material properties of the FGM beam will be more dominated by the metal as the volume fraction exponent increases, which leads to decrease of the system stiffness. Similarly, the location of the lumped mass also has effects on the system stiffness. The first natural frequency decreases when the location of the lumped mass approaches the tip of the FGM-PZT beam, which is consistent with the conclusion obtained in literature [36]. As it can be seen from the

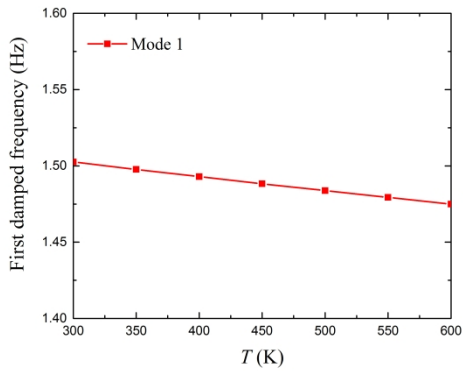
table, the increases of the values of  $N$  and  $l_l$  will cause the system become softer.

Figs. 14(a)-(f) show the influence of temperature on the first three damped natural frequencies and damping ratios of the rotating FGM-PZT beam when  $\Omega = 200$  rpm,  $N=0.5$ ,  $K_p=1$  and  $K_d=-10$ . The temperature field varies from  $T=300$  K to  $T=600$  K. As shown in Figs. 14(a), 14(c) and 14(e), the damped natural frequencies of the first three modes gradually decrease with increasing temperature linearly. In Figs. 14(b), 14(d) and 14(f), the first damping ratio of the FGM-PZT beam increases with increasing temperature, while the second and third damping ratios decrease with increasing temperature. The system becomes softer due to the decrease of system stiffness when the temperature increases. Since the temperature dependent material properties are changed with the temperature, the slight changes of the structural damping of the FGM beam can be observed. It is indicated that the effect of temperature variation on the free vibration characteristics of the rotating smart structure is quite gentle despite non-negligibility.

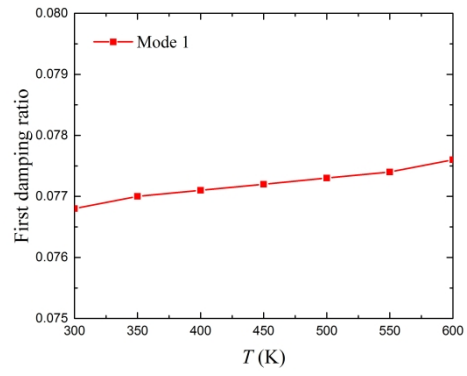
Table 5. Effect of the volume fraction exponent  $N$  and location of the lumped mass on the natural frequencies of the first mode of the rotating smart beam when  $\Omega = 200$  rpm ;

$$K_p = K_d = 0 ; T = 300 \text{ K} .$$

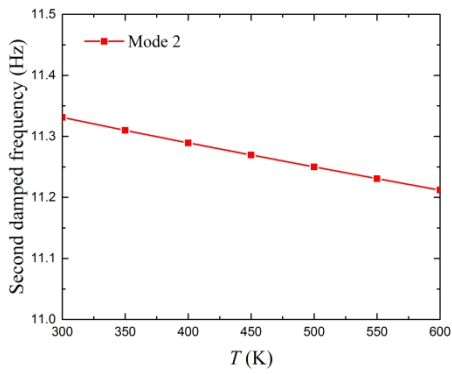
$N$	$l_l$ (m)	1st natural frequency (Hz)
0.5	1	1.4947
	2	1.4941
	3	1.4915
	4	1.4865
	5	1.4793
1	1	1.4623
	2	1.4616
	3	1.4589
	4	1.4538
	5	1.4463
2	1	1.4439
	2	1.4432
	3	1.4404
	4	1.4350
	5	1.4271



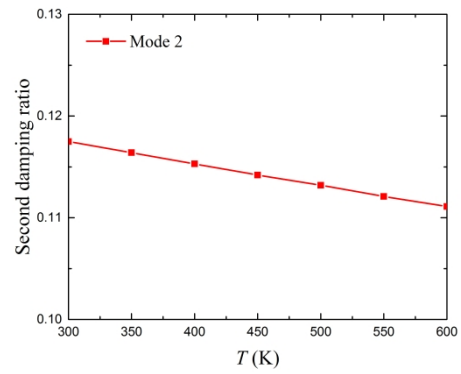
(a)



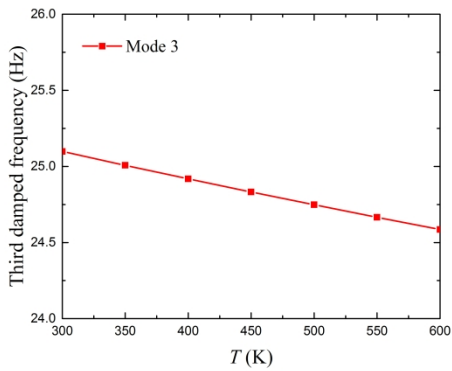
(b)



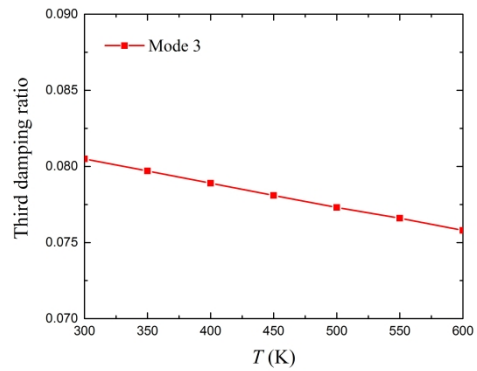
(c)



(d)



(e)



(f)

Fig. 14. Influence of temperature on the damped natural frequencies of the first three modes and damping ratios of the first three modes of the rotating smart beam when  $\Omega = 200$  rpm ;

$$N=0.5; K_p=1, K_d=-10.$$

Figs. 15(a) and 15(b) show variations of the damped frequency and the damping ratio of the first mode of the smart beam when  $\Omega = 200$  rpm in different temperature field with the proportional control gain  $K_p$  when  $N = 1$ , respectively. It can be seen from Fig. 15(b) that the damping effect caused by  $K_p$  is enhanced when the temperature is increased. Since the order of magnitude of the damping ratio is  $10^{-4}$ - $10^{-3}$ , the damping effect caused by  $K_p$  is quite small. Figs. 16(a) and 16(b) show variations of the damped frequency and the damping ratio of the first mode of the smart beam when  $\Omega = 200$  rpm in different temperature field with the absolute value of proportional control gain  $K_d$  when  $N = 1$ , respectively. The damping ratio of the first mode of the smart beam increases first and then decreases with the increasing  $|K_d|$ . The order of magnitude of the damping ratio is  $10^{-2}$ - $10^{-1}$ , which shows that the damping effect caused by  $K_d$  is more significant than that caused by  $K_p$ .

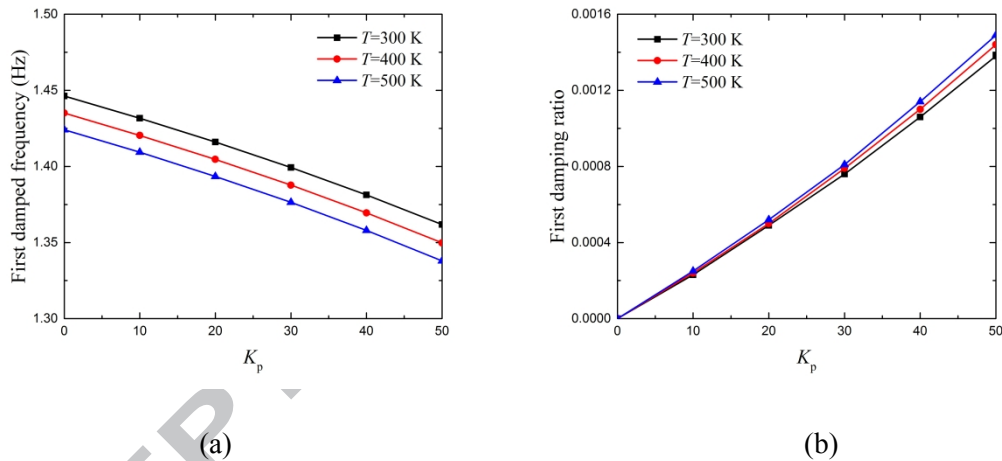


Fig. 15. Variations of (a) the damped frequency and (b) the damping ratio of the first mode of the smart beam in different temperature field when  $\Omega = 200$  rpm with the proportional control gain  $K_p$ ;  $N = 1$ .

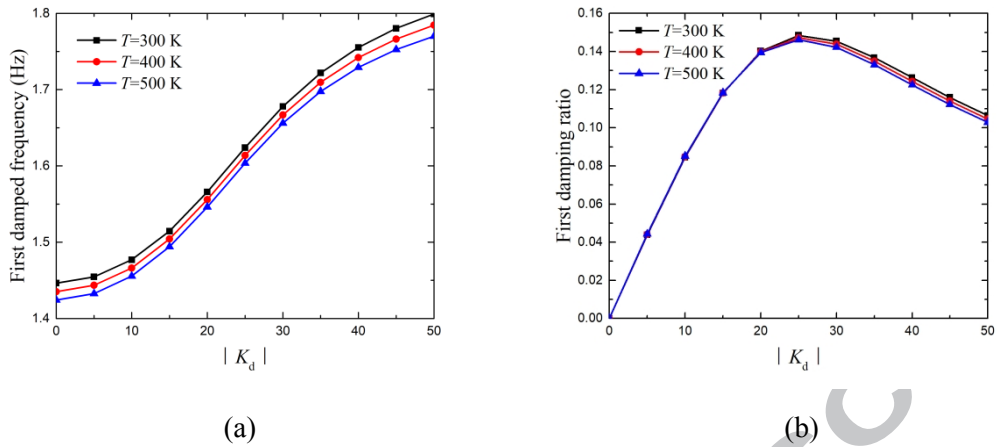


Fig. 16. Variations of (a) the damped frequency and (b) the damping ratio of the first mode of the smart beam in different temperature field when  $\Omega = 200$  rpm with  $|K_d|$ ;  $N = 1$ .

Figs. 17(a) and 17(b) show variations of the damped frequencies and damping ratios of the first three modes of the smart beam with the angular velocity when  $K_p = 0$ ,  $K_d = -20$ ,  $T = 500$  K, and  $N = 1$ , respectively. As it can be seen from the results, the damped frequencies of the first three modes increase with the increase of the angular velocity due to the effect of dynamic stiffening. The damping ratios of the first three modes decrease as the angular velocity increase, which indicates that a larger value of control gain should be selected when the beam rotates at a higher speed to ensure the vibration suppression performance.

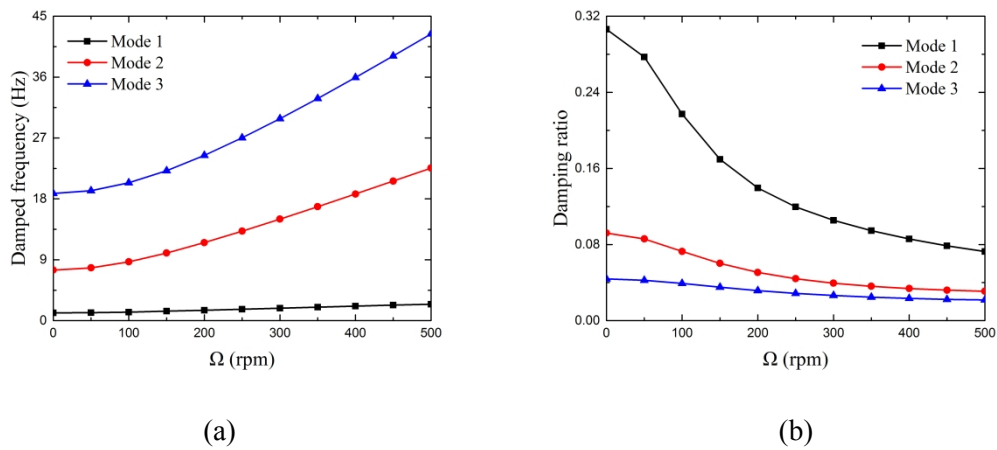


Fig. 17. Variations of (a) the damped frequencies and (b) the damping ratios of the first three modes of the smart beam with the angular velocity when  $K_p = 0$ ,  $K_d = -20$ ,  $T = 500$  K, and  $N = 1$ .

#### 4 Conclusion

Vibration control and analysis of a rotating FGM beam with a lumped mass and bonded piezoelectric films in temperature field were investigated. The thermo-electro-mechanical dynamic model of the smart system was developed based on the HOC modeling theory. Equations of motion of the system were derived by employing Lagrange's equations. The characteristics of the active control of the thermally induced vibration of the rotating FGM beam were investigated. According to the numerical results, the cost of the vibration control can be reduced by selecting the control gain properly. The influence of high-order nonlinearity in the present HOC model on the behaviors of dynamics and control of flexible structures in thermal environment should be included. The effect of temperature variation on the free vibration characteristics of the rotating smart structure is quite gentle despite non-negligibility. Besides, parameters such as the volume fraction exponent of the FGM beam, the location of the lumped mass and the angular velocity of the hub have significant impacts on the dynamic behaviors of the system. The results of this paper can be used to provide theoretical basis for vibration and control analysis for blades, robot arms, and other rotary flexible structures operating in high temperature field.

#### Acknowledgements

This research is funded by the Hong Kong Scholars Program (Project No. XJ2017021) and the grants from the National Natural Science Foundation of China (Project Nos. 11502113 and 11772158) and the grant from the Natural Science Foundation of Jiangsu Province (Project No. BK20170820).

#### Appendix A

In Eq. (39)

$$\begin{aligned}
 M_{11} = & J_{oh} + J_{ob} + 2S_x A + A^T M_x A + B^T M_y B - \underline{B^T C B} + \frac{1}{2} (h + h_p)^2 \rho_p A_p B^T M_{yy} B \\
 & + \frac{1}{4} \int_0^l (\rho A + 2\rho_p A_p) (\underline{B^T H B B^T H B}) dx - \int_0^l (\rho A + 2\rho_p A_p) (\underline{A^T \Phi_x^T B^T H B}) dx \\
 & + \frac{1}{4} m_l [\underline{B^T H(l) B B^T H(l) B}] + \frac{1}{4} \int_0^l \rho b h (\underline{B^T H B B^T H B}) dx \\
 & - \int_0^l \rho b h (\underline{A^T \Phi_x^T B^T H B}) dx - m_l [\underline{A^T \Phi_x^T(l) B^T H(l) B}]
 \end{aligned} \tag{A1}$$

$$M_{22} = M_x \tag{A2}$$

$$M_{33} = M_y + \int_0^l (\rho A + 2\rho_p A_p) (\underline{H B B^T H}) dx + m_l [\underline{H(l) B B^T H(l)}] \tag{A3}$$

$$\mathbf{M}_{21} = \mathbf{M}_{12}^T = -\mathbf{M}_{xy} \mathbf{B} \quad (\text{A4})$$

$$\begin{aligned} \mathbf{M}_{31} = \mathbf{M}_{13}^T = \mathbf{S}_y^T + \mathbf{M}_{xy}^T \mathbf{A} + \mathbf{Y}^T + \int_0^l (\rho A + 2\rho_p A_p) \left( \mathbf{H} \mathbf{B} \Phi_y \mathbf{B} - \frac{1}{2} \Phi_y^T \mathbf{B}^T \mathbf{H} \mathbf{B} \right) dx \\ + m_l \left[ \mathbf{H}(l_l) \mathbf{B} \Phi_y(l_l) \mathbf{B} - \frac{1}{2} \Phi_y^T(l_l) \mathbf{B}^T \mathbf{H}(l_l) \mathbf{B} \right] \end{aligned} \quad (\text{A5})$$

$$\mathbf{M}_{32} = \mathbf{M}_{23}^T = -\int_0^l (\rho A + 2\rho_p A_p) (\mathbf{H} \mathbf{B} \Phi_x) dx - m_l [\mathbf{H}(l_l) \mathbf{B} \Phi_x(l_l)] \quad (\text{A6})$$

$$\begin{aligned} \mathcal{Q}_\theta = \tau - 2\dot{\theta}_0 \left[ \mathbf{S}_x \dot{\mathbf{A}} + \mathbf{A}^T \mathbf{M}_x \dot{\mathbf{A}} + \mathbf{B}^T \mathbf{M}_y \dot{\mathbf{B}} - \mathbf{B}^T \mathbf{C} \dot{\mathbf{B}} + \frac{1}{2} (h + h_p)^2 \rho_p A_p \mathbf{B}^T \mathbf{M}_{yy} \dot{\mathbf{B}} \right] \\ - \int_0^l (\rho A + 2\rho_p A_p) (\mathbf{B}^T \Phi_y^T \dot{\mathbf{B}}^T \mathbf{H} \mathbf{B}) dx + \dot{\theta}_0 \int_0^l (\rho A + 2\rho_p A_p) (\dot{\mathbf{A}}^T \Phi_x^T \mathbf{B}^T \mathbf{H} \mathbf{B} \\ + 2\mathbf{A}^T \Phi_x^T \mathbf{B}^T \mathbf{H} \dot{\mathbf{B}} - \mathbf{B}^T \mathbf{H} \mathbf{B} \dot{\mathbf{B}}^T \mathbf{H} \mathbf{B}) dx - m_l [\mathbf{B}^T \Phi_y^T(l_l) \dot{\mathbf{B}}^T \mathbf{H}(l_l) \dot{\mathbf{B}}] \\ + \dot{\theta}_0 m_l [\dot{\mathbf{A}}^T \Phi_x^T(l_l) \mathbf{B}^T \mathbf{H}(l_l) \mathbf{B} + 2\mathbf{A}^T \Phi_x^T(l_l) \mathbf{B}^T \mathbf{H}(l_l) \dot{\mathbf{B}} - \mathbf{B}^T \mathbf{H}(l_l) \mathbf{B} \dot{\mathbf{B}}^T \mathbf{H}(l_l) \dot{\mathbf{B}}] \end{aligned} \quad (\text{A7})$$

$$\begin{aligned} \mathcal{Q}_A = \mathcal{Q}_{pf} + \mathcal{Q}_{T1} + \dot{\theta}_0^2 [\mathbf{S}_x^T + \mathbf{M}_x \mathbf{A}] + 2\dot{\theta}_0 \mathbf{M}_{xy} \dot{\mathbf{B}} - (E_{A1} b + 2E_p A_p) \mathbf{K}_1 \mathbf{A} + \mathbf{K}_2 \mathbf{B} \\ - \frac{1}{2} \dot{\theta}_0^2 \int_0^l (\rho A + 2\rho_p A_p) (\Phi_x^T \mathbf{B}^T \mathbf{H} \mathbf{B}) dx + \int_0^l (\rho A + 2\rho_p A_p) (\Phi_x^T \dot{\mathbf{B}}^T \mathbf{H} \mathbf{B}) dx \\ - \frac{1}{2} \dot{\theta}_0^2 m_l [\Phi_x^T(l_l) \mathbf{B}^T \mathbf{H}(l_l) \mathbf{B}] + \int_0^l \rho b (\Phi_x^T \dot{\mathbf{B}}^T \mathbf{H} \mathbf{B}) dx + m_l [\Phi_x^T(l_l) \dot{\mathbf{B}}^T \mathbf{H}(l_l) \dot{\mathbf{B}}] \end{aligned} \quad (\text{A8})$$

$$\begin{aligned} \mathcal{Q}_B = \mathcal{Q}_{pm} + \mathcal{Q}_{T2} + \dot{\theta}_0^2 (\mathbf{M}_y - \mathbf{C}) \mathbf{B} - 2\dot{\theta}_0 \mathbf{M}_{xy}^T \dot{\mathbf{A}} - \mathbf{K}_3 \mathbf{B} + \mathbf{K}_2^T \mathbf{A} + \frac{1}{2} (1 + \dot{\theta}_0^2) (h + h_p)^2 \rho_p A_p \mathbf{M}_{yy} \mathbf{B} \\ + \dot{\theta}_0^2 \int_0^l (\rho A + 2\rho_p A_p) \left( \frac{1}{2} \mathbf{H} \mathbf{B} \mathbf{B}^T \mathbf{H} \mathbf{B} - \mathbf{H} \mathbf{B} \Phi_x \mathbf{A} \right) dx - 2\dot{\theta}_0 \int_0^l [(\rho A + 2\rho_p A_p) \mathbf{H} \mathbf{B} \Phi_y \dot{\mathbf{B}} \\ - \Phi_y^T \mathbf{B}^T \mathbf{H} \dot{\mathbf{B}}] dx - \int_0^l (\rho A + 2\rho_p A_p) (\mathbf{H} \mathbf{B} \dot{\mathbf{B}}^T \mathbf{H} \mathbf{B}) dx + \dot{\theta}_0^2 m_l \left[ \frac{1}{2} \mathbf{H}(l_l) \mathbf{B} \mathbf{B}^T \mathbf{H}(l_l) \mathbf{B} - \mathbf{H}(l_l) \mathbf{B} \Phi_x(l_l) \mathbf{A} \right] \\ - 2\dot{\theta}_0 \int_0^l \rho b (\mathbf{H} \mathbf{B} \Phi_y \dot{\mathbf{B}} - \Phi_y^T \mathbf{B}^T \mathbf{H} \dot{\mathbf{B}}) dx - 2\dot{\theta}_0 m_l [\mathbf{H}(l_l) \mathbf{B} \Phi_y(l_l) \dot{\mathbf{B}} - \Phi_y^T(l_l) \mathbf{B}^T \mathbf{H}(l_l) \dot{\mathbf{B}}] \\ - \int_0^l \rho b (\mathbf{H} \mathbf{B} \dot{\mathbf{B}}^T \mathbf{H} \mathbf{B}) dx - m_l [\mathbf{H}(l_l) \mathbf{B} \dot{\mathbf{B}}^T \mathbf{H}(l_l) \dot{\mathbf{B}}] \end{aligned} \quad (\text{A9})$$

in which

$$J_{ob} = \int_0^l (\rho A + 2\rho_p A_p) (R + x)^2 dx + (R + l_l)^2 m_l \quad (\text{A10})$$

$$\mathbf{Y} = \int_{V_f} \rho(y) y^2 \Phi_y' dV_f \quad (\text{A11})$$

$$\mathbf{S}_x = \int_0^l (\rho A + 2\rho_p A_p) (R + x) \Phi_x dx + (R + l_l) \Phi_x(l_l) m_l \quad (\text{A12})$$

$$\mathbf{S}_y = \int_0^l (\rho A + 2\rho_p A_p) (R + x) \Phi_y dx + (R + l_l) \Phi_y(l_l) m_l \quad (\text{A13})$$

$$\mathbf{M}_x = \int_0^l (\rho A + 2\rho_p A_p) \Phi_x^T \Phi_x dx + \Phi_x^T(l_l) \Phi_x(l_l) m_l \quad (\text{A14})$$

$$\mathbf{M}_y = \int_0^l (\rho A + 2\rho_p A_p) \boldsymbol{\Phi}_y^T \boldsymbol{\Phi}_y dx + \int_{V_f} \rho(y) y^2 \boldsymbol{\Phi}_y^T(x) \boldsymbol{\Phi}_y'(x) dV_f + \boldsymbol{\Phi}_y^T(l) \boldsymbol{\Phi}_y(l) m_l \quad (\text{A15})$$

$$\mathbf{M}_{yy} = \int_0^l \boldsymbol{\Phi}_y^T \boldsymbol{\Phi}_y' dx + \boldsymbol{\Phi}_x^T(l) \boldsymbol{\Phi}_y(l) m_l \quad (\text{A16})$$

$$\mathbf{M}_{xy} = \int_0^l (\rho A + 2\rho_p A_p) \boldsymbol{\Phi}_x^T \boldsymbol{\Phi}_y dx + \boldsymbol{\Phi}_x^T(l) \boldsymbol{\Phi}_y(l) m_l \quad (\text{A17})$$

$$\mathbf{C} = \int_0^l (\rho A + 2\rho_p A_p) (R + x) \mathbf{H} dx + (R + l) \mathbf{H}(l) m_l \quad (\text{A18})$$

$$\mathbf{K}_1 = \int_0^l \boldsymbol{\Phi}_x^T \boldsymbol{\Phi}_x' dx \quad (\text{A19})$$

$$\mathbf{K}_2 = \int_0^l E_{A2} b \boldsymbol{\Phi}_x^T \boldsymbol{\Phi}_y'' dx \quad (\text{A20})$$

$$\mathbf{K}_3 = \int_0^l \left[ E_{A3} b + E_p A_p \left( \frac{h^2}{4} + \frac{hh_p}{2} + \frac{h_p^2}{3} \right) \right] \boldsymbol{\Phi}_y^T \boldsymbol{\Phi}_y'' dx \quad (\text{A21})$$

$$\rho = \frac{\int_{\frac{h}{2}}^h \rho(y) dy}{h} = \frac{(\rho_c - \rho_m)}{N+1} + \rho_m \quad (\text{A22})$$

$$E_{A1} = \int_{\frac{h}{2}}^h E(y, T) dy \quad (\text{A23})$$

$$E_{A2} = \int_{\frac{h}{2}}^h E(y, T) y dy \quad (\text{A24})$$

$$E_{A3} = \int_{\frac{h}{2}}^h E(y, T) y^2 dy \quad (\text{A25})$$

## Appendix B

In Eq. (40)

$$\mathbf{K}_{22} = (E_{A1} b + 2E_p A_p) \mathbf{K}_1 - \Omega^2 \mathbf{M}_x \quad (\text{B1})$$

$$\mathbf{G}_{23} = -g K_d \int_0^l \boldsymbol{\Phi}_x^T \left( \int_0^l \boldsymbol{\Phi}_y'' dx \right) dx - 2\Omega \mathbf{M}_{xy} \quad (\text{B2})$$

$$\mathbf{G}_{32} = 2\Omega \mathbf{M}_{xy}^T \quad (\text{B3})$$

$$\mathbf{G}_{33} = -d_0 g K_d \int_0^l \boldsymbol{\Phi}_y^T \left( \int_0^l \boldsymbol{\Phi}_y'' dx \right) dx \quad (\text{B4})$$

$$\mathbf{K}_{23} = -g K_p \int_0^l \boldsymbol{\Phi}_x^T \left( \int_0^l \boldsymbol{\Phi}_y'' dx \right) dx - \mathbf{K}_2 \quad (\text{B5})$$

$$\mathbf{K}_{32} = -\mathbf{K}_2^T \quad (\text{B6})$$

$$\mathbf{K}_{33} = -d_0 g K_p \int_0^l \boldsymbol{\Phi}_y^T \left( \int_0^l \boldsymbol{\Phi}_y'' dx \right) dx + \Omega^2 (\mathbf{C} - \mathbf{M}_y) - \frac{1}{2} (1 + \Omega^2) (h + h_p)^2 \rho_p A_p \mathbf{M}_{yy} + \mathbf{K}_3 \quad (\text{B7})$$

**References**

- [1] A. Gupta, M. Talha, Recent development in modeling and analysis of functionally graded materials and structures, *Prog. Aerosp. Sci.* 79 (2015) 1-14.
- [2] X.Q. He, T.Y. Lam, K.M. Liew, Active control of FGM plates with integrated piezoelectric sensors and actuators, *Int. J. Solids Struct.* 38 (2001) 1641-1655.
- [3] K.M. Liew, J. Yang, S. Kitipornchai, Postbuckling of piezoelectric FGM plates subject to thermo-electro-mechanical loading, *Int. J. Solids Struct.* 40 (2003) 3869-3892.
- [4] X.L. Huang, H.S. Shen, Vibration and dynamic response of functionally graded plates with piezoelectric actuators in thermal environments, *J. Sound Vib.* 289 (2006) 25-53.
- [5] H.S. Shen, Nonlinear thermal bending response of FGM plates due to heat conduction, *Compos. Part B-Eng.* 38 (2007) 201-215.
- [6] V. Fakhari, A. Ohadi, P. Yousefian, Nonlinear free and forced vibration behavior of functionally graded plate with piezoelectric layers in thermal environment, *Compos. Struct.* 93 (2011) 2310-2321.
- [7] X.L. Jia, L.L. Ke, X.L. Zhong, Y. Sun, J. Yang, S. Kitipornchai. Thermal-mechanical-electrical buckling behavior of functionally graded micro-beams based on modified couple stress theory, *Compos. Struct.* (2018), <https://doi.org/10.1016/j.compstruct.2018.03.025>.
- [8] Z.X Wang, H.S. Shen. Nonlinear vibration of sandwich plates with FG-GRC face sheets in thermal environments, *Compos. Struct.* 192 (2018) 642-653.
- [9] L. Librescu, S.Y. Oh, O. Song, Spinning thin-walled beams made of functionally graded materials: Modeling, vibration and instability, *Eur. J. Mech. A-Solid.* 23 (2004) 499-515.
- [10] S.A. Fazelzadeh, P. Malekzadeh, P. Zahedinejad, M. Hosseini, Vibration analysis of functionally graded thin-walled rotating blades under high temperature supersonic flow using the differential quadrature method, *J. Sound Vib.* 306 (2007) 333-348.
- [11] M.T. Piovan, R. Sampaio, A study on the dynamics of rotating beams with functionally graded properties, *J. Sound Vib.* 327 (2009) 134-143.
- [12] H. Zarrinzadeh, R. Attarnejad, A. Shahba, Free vibration of rotating axially functionally graded tapered beams, *P. I. Mech. Eng. G-J. Aer.* 226 (2012) 363-379.
- [13] L. Li, D.G. Zhang, W.D. Zhu, Free vibration analysis of a rotating hub-functionally graded material beam system with the dynamic stiffening effect, *J. Sound Vib.* 333 (2014) 1526-1541.
- [14] L. Li, D.G. Zhang, Free vibration analysis of rotating functionally graded rectangular plates, *Compos. Struct.* 136 (2016) 493-504.
- [15] Y. Oh, H.H. Yoo, Vibration analysis of rotating pretwisted tapered blades made of functionally graded materials, *Int. J. Mech. Sci.* 119 (2016) 68-79.
- [16] A. Baz, S. Poh, Performance of an active control system with piezoelectric actuators, *J. Sound Vib.* 126 (1988) 327-343.
- [17] W.H. Liao, K.W. Wang, On the active-passive hybrid control actions of structures with

- active constrained layer treatments, *J. Vib. Acoust.* 119 (1997) 563-572.
- [18] F.M. Li, X.X. Lyu, Active vibration control of lattice sandwich beams using the piezoelectric actuator/sensor pairs, *Compos. Part B-Eng.* 67 (2014) 571-578.
- [19] J. Maruani, I. Bruant, F. Pablo, L. Gallimard. A numerical efficiency study on the active vibration control for a FGPM beam, *Compos. Struct.* 182 (2017) 478-486.
- [20] X.M. Wang, W.Y. Zhou, Z.G. Wu, Feedback tracking control for dynamic morphing of piezocomposite actuated flexible wings, *J. Sound Vib.* 416 (2018) 17-28.
- [21] Y.Y. Chai, Z.G. Song, F.M. Li, Active aerothermoelastic flutter suppression of composite laminated panels with time-dependent boundaries, *Compos. Struct.* 179 (2017) 61-76.
- [22] S.B. Choi, M.S. Han, Vibration control of a rotating cantilevered beam using piezoactuators: experimental work, *J. Sound Vib.* 277 (2004) 436-442.
- [23] D. Sun, J.K. Mills, Control of a rotating cantilever beam using a torque actuator and a distributed piezoelectric polymer actuator, *Appl. Acoust.* 63 (2002) 885-899.
- [24] Y.A. Huang, Z.C. Deng, Y.L. Xiong, High-order model and slide mode control for rotating flexible smart structure, *Mech. Mach. Theory.* 43 (2008) 1038-1054.
- [25] S.C. Choi, J.S. Park, J.H. Kim, Vibration control of pre-twisted rotating composite thin-walled beams with piezoelectric fiber composites, *J. Sound Vib.* 300 (2007) 176-196.
- [26] X. Wang, M. Morandini, P. Masarati, Modeling and control for rotating pretwisted thin-walled beams with piezo-composite, *Compos. Struct.* 180 (2017) 647-663.
- [27] N.K. Chandiramani, Active control of a piezo-composite rotating beam using coupled plant dynamics, *J. Sound Vib.* 329 (2010) 2716-2737.
- [28] M. Bodaghi, A.R. Damanpack, M.M. Aghdam, M. Shakeri, Non-linear active control of FG beams in thermal environments subjected to blast loads with integrated FGP sensor/actuator layers, *Compos. Struct.* 94 (2012) 3612-3623.
- [29] B.A. Selim, L.W. Zhang, K.M. Liew, Active vibration control of FGM plates with piezoelectric layers based on Reddy's higher-order shear deformation theory, *Compos. Struct.* 155 (2016) 118-134.
- [30] L.W. Zhang, Z.G. Song, K.M. Liew, Modeling aerothermoelastic properties and active flutter control of nanocomposite cylindrical shells in supersonic airflow under thermal environments, *Comput. Method Appl. M.* 325 (2017) 416-433.
- [31] P. Phung-Van, T. Nguyen-Thoi, T. Le-Dinh, H. Nguyen-Xuan, Static and free vibration analyses and dynamic control of composite plates integrated with piezoelectric sensors and actuators by the cell-based smoothed discrete shear gap method (CS-FEM-DSG3), *Smart Mater. Struct.* 22 (2013) 095026.
- [32] P. Phung-Van, L.D. Lorenzis, C.H. Thai, M. Abdel-Wahab, H. Nguyen-Xuan, Analysis of laminated composite plates integrated with piezoelectric sensors and actuators using higher-order shear deformation theory and isogeometric finite elements, *Comp. Mater. Sci.* 96 (2015) 495-505.

- [33] P. Phung-Van, M. Abdel-Wahab, K.M. Liew, S.P.A. Bordas, H. Nguyen-Xuan, Isogeometric analysis of functionally graded carbon nanotube-reinforced composite plates using higher-order shear deformation theory, *Compos. Struct.* 123 (2015) 137-149.
- [34] P. Phung-Van, L.B. Nguyen, L.V. Tran, T.D. Dinh, C.H. Thai, S.P.A. Bordas, An efficient computational approach for control of nonlinear transient response of smart piezoelectric composite plates, *Int. J. Nonlin. Mech.* 76 (2015) 190-202.
- [35] P. Phung-Van, L.V. Tran, A.J.M. Ferreira, H. Nguyen-Xuan, M. Abdel-Wahab, Nonlinear transient isogeometric analysis of smart piezoelectric functionally graded material plates based on generalized shear deformation theory under thermo-electro-mechanical loads, *Nonlinear Dyn.* 87 (2017) 879-894.
- [36] T. Aksencer, M. Aydogdu, Vibration of a rotating composite beam with an attached point mass, *Compos. Struct.* 190 (2018) 1-9.
- [37] H.S. Shen, Nonlinear bending of functionally graded carbon nanotube-reinforced composite plates in thermal environments, *Compos. Struct.* 91 (2009) 9-19.
- [38] R. Javaheri, M.R. Eslami, Thermal buckling of functionally graded plates, *AIAA J.* 40 (2002) 162-169.
- [39] J.N. Reddy, C.D. Chin, Thermoelastical analysis of functionally graded cylinders and plates, *J. Therm. Stresses* 21 (1998): 593–626.
- [40] E.H.K. Fung, J.Q. Zou, H.W.J. Lee, Lagrangian formulation of rotating beam with active constrained layer damping in time domain analysis, *J. Mech. Design.* 126 (2004) 359-364.
- [41] A. Baz, J. Ro, Vibration control of rotating beams with active constrained layer damping, *Smart Mater. Struct.* 10 (2001) 112-120.
- [42] M. Azadi, Free and forced vibration analysis of FG beam considering temperature dependency of material properties, *J. Mech. Sci. Technol.* 25 (2011) 69-80.